

Automated localization and segmentation techniques for B-mode ultrasound images: A review

Original

Automated localization and segmentation techniques for B-mode ultrasound images: A review / Meiburger, Kristen M.; Acharya, U. Rajendra; Molinari, Filippo. - In: COMPUTERS IN BIOLOGY AND MEDICINE. - ISSN 0010-4825. - STAMPA. - 92:(2018), pp. 210-235. [10.1016/j.combiomed.2017.11.018]

Availability:

This version is available at: 11583/2701831 since: 2022-06-14T10:24:08Z

Publisher:

Elsevier Ltd

Published

DOI:10.1016/j.combiomed.2017.11.018

Terms of use:

This article is made available under terms and conditions as specified in the corresponding bibliographic description in the repository

Publisher copyright

Elsevier preprint/submitted version

Preprint (submitted version) of an article published in COMPUTERS IN BIOLOGY AND MEDICINE © 2018,
<http://doi.org/10.1016/j.combiomed.2017.11.018>

(Article begins on next page)

Automated localization and segmentation techniques for B-mode ultrasound images: a review

Kristen M. Meiburger¹, U Rajendra Acharya^{2,3,4}, Filippo Molinari¹

¹Biolab, Department of Electronics and Telecommunications, Politecnico di Torino, Torino, Italy

²Department of Electronic & Computer Engineering, Ngee Ann Polytechnic, Singapore

³Department of Biomedical Engineering, School of Science and Technology, SUSS University, Singapore

⁴Department of Biomedical Imaging, Faculty of Medicine, University of Malaya, Kuala Lumpur, Malaysia

Abstract

B-mode ultrasound imaging is used extensively in medicine. Hence, there is a need to have efficient segmentation tools to aid in computer-aided diagnosis, image-guided interventions, and therapy. This paper presents a comprehensive review on automated localization and segmentation techniques for B-mode ultrasound images. The paper first describes the general characteristics of B-mode ultrasound images. Then insight on the localization and segmentation of tissues is provided, both in the case in which the organ/tissue localization provides the final segmentation and in the case in which a two-step segmentation process is needed, due to the desired boundaries being too fine to locate from within the entire ultrasound frame. In this section, examples of some main techniques found in literature are shown, including but not limited to shape priors, superpixel and classification, local pixel statistics, active contours, edge-tracking, dynamic programming, and data mining. Ten selected applications (abdomen/kidney, breast, cardiology, thyroid, liver, vascular, musculoskeletal, obstetrics, gynecology, prostate) are then investigated in depth, and the performances of a few specific applications are compared. In conclusion, future perspectives for B-mode based segmentation, such as the integration of RF information, the employment of higher frequency probes when possible, the focus on completely automatic algorithms, and the increase in available data are discussed.

Keywords: ultrasound, automated, localization, segmentation, B-mode imaging, review

1. Introduction and overview

B-mode ultrasound imaging is widely used in medicine as a diagnostic tool. It is capable of acquiring images in real-time, uses non-ionizing radiation, presents no risk to patients, and is inexpensive compared to other imaging modalities [1].

An ultrasound B-mode image results from various physical phenomena. In particular, a short ultrasound pulse is emitted from the probe, and some waves are then reflected back to the transducer after encountering a tissue with different acoustic impedance, while the rest penetrate deeper into the tissue. The back scattered ultrasound waves are then electronically detected again by the probe and displayed as an image, where the intensity is proportional to the strength of the return echo [1].

Ultrasound imaging continues to grow and advances are continuously being made in transducer design, digital systems, spatial/temporal resolution, and portability. Alongside these developments, ultrasound

image processing and segmentation also continue to find their place in providing an important tool in computer-aided diagnosis, therapy, and image-guided interventions.

More recently, the importance of providing fully automated localization and segmentation techniques has shown to be a hot topic in ultrasound, as the amount of data to be analyzed continues to grow and the capability of processing large multi-institutional databases proves to be an asset for large projects and studies. Clinically, these techniques can also aid in the diagnosis and treatment of patients, providing both a tool for locating potential areas of interest and for quantitatively measuring important clinical information. Automated localization techniques refer to those methods that provide an initial segmentation and localization of an object of interest within which a fine segmentation technique is used to obtain the final quantitative information. Depending on the specific application, fine segmentation techniques can be employed within a determined ROI or on the entire ultrasound frame without the use of a localization method to first isolate the general area.

A few reviews and surveys have been done regarding ultrasound image segmentation [2], [3], and many reviews are found when considering specific clinical applications [4]–[7]. However, to the best of our knowledge, this is the first thorough review on automated localization and segmentation techniques for B-mode ultrasound images. Importantly, this review provides insight on both coarse localization and fine segmentation techniques, analyzing the various methods' robustness to noise and artifacts. This review can serve as a manual for the numerous types of ultrasound B-mode segmentation algorithms and clearly states the advantages and disadvantages of the different methods. It is important to note that in this review only B-mode ultrasound image segmentation techniques are considered. The techniques based on color, Doppler ultrasound images, elasticity images, or functional ultrasound contrast image sequences are not considered.

The overview of this review is as follows. The second section reports the general characteristics of B-Mode ultrasound images and challenges these images may present for automatic segmentation techniques. The third section describes the main coarse localization and fine segmentation techniques found in literature, describing when a method can be used for either coarse localization or fine segmentation or both. The fourth section concentrates on selected possible applications, providing a brief overview of recent techniques in their corresponding specific fields. Quantitative performance results are compared and investigated for a few specific applications. A discussion on the methods and clinical applications presented and future perspectives of B-mode ultrasound image segmentation concludes the paper.

2. General characteristics and challenges of B-mode ultrasound images and the role of image pre-processing

The ultrasound display equipment depends on specific physical assumptions to allocate the intensity and location of each received echo during the construction of the ultrasound (US) B-mode image. When these certain assumptions are not met, echoes can be displayed erroneously in the B-mode image and perceived as artifacts in the image. It is important to understand some of these basic artifacts before diving deeper into automatic ultrasound image analysis as these artifacts can affect the way strategies and methods perform. Briefly, when the detected echoes do not actually originate from within the main ultrasound beam, a beam width artifact or side lobe artifact can be noticed in the B-mode image [8]. These phenomena can be identified as extraneous echoes that are present within an expected anechoic structure. Similarly, US image formation presumes that an echo returns back to the transducer after one reflection and how deep the object is found is directly related to the time elapsed for the round trip. When this

assumption is not met, various artifacts such as *reverberation*, *comet tail*, *ring-down*, *mirror image*, producing multiple echoes deriving from the same structure are produced. B-mode ultrasound image formation also assumes that the speed of sound is constant in all human tissues; when imaging a tissue that has a speed of ultrasound significantly different from the assumed average value (1540 m/s), echoes can be displayed either deeper or shallower in the image, depending on if the actual velocity is either slower or faster than the average assumed value. Similarly, when there is a change in the velocity between adjacent tissues, a *refraction* artifact may be produced. Finally, the last type of artifact is formed when the ultrasound beam comes across a focal material that attenuates either more or less when compared to the surrounding tissue. This phenomenon produces the well-known *shadowing effect* below the high-absorbing tissue and *bright band effect* below the low-absorbing tissue.

All of the ultrasound artifacts described above can have different appearances in images based on the operator that acquires the image, which is a first main challenge with ultrasound imaging: it is heavily user-dependent. B-mode images of the same tissue acquired by different users can be visually different, if different gain settings and time-gain compensation settings are used. This can be mitigated by using the same imaging presets whenever possible.

An important feature for all types of imaging modalities is *image resolution*. In ultrasound imaging, image resolution is directly related to the transducer frequency, if the same pulse duration is considered. High-frequency ultrasound waves generate images with a higher axial resolution; however, when considering a given distance, low-frequency waves attenuate less than high-frequency waves. High frequency (10-15MHz) and low-frequency (2-5 MHz) transducers are preferred to scan superficial and deeper structures respectively [1].

B-mode ultrasound images can be distinguished from other imaging techniques due to the presence of speckle, a typical granular appearance in US images. Speckle presents both a deterministic and a random nature because it is created from the reflected echoes of either coherently or randomly distributed tissue scatterers [9]. The signal that is received (therefore also the echo envelope) exhibits statistical properties that are determined by important factors, such as the scatterer spatial distribution and density in the tissue.

The scattered waves deriving from different scatterers interfere when multiple small scatterers are present in an insonifying ultrasound pulse. The interference pattern is random because the scatterers spacing between each other is also random, producing in some locations a constructive pattern (generating a bright spot in the image) and in other adjacent locations a destructive pattern (generating a dark spot). The resulting pattern then produces this “grainy” speckle effect.

Speckle contains important information on scatterer statistics and is fundamental for many techniques that have been developed for the real-time tracking of structures, where a specific speckle pattern is followed in time [10], [11]. Still, when considering the automatic localization and segmentation in non-temporal B-mode ultrasound images, speckle is typically considered to be an image-degrading artifact [12]. In fact, much research effort is precisely aimed at developing effective methods in minimizing the speckle artifact while maintaining the true detail of the morphology in the image.

Image Preprocessing

As can be seen from the previous paragraphs, there are various challenges that present a hurdle to be overcome when segmenting B-mode ultrasound images. Image pre-processing techniques can mitigate some of these issues and should be employed when possible.

A way to partially overcome user-dependency in ultrasound images is to intensity normalize the image so as to exploit the entire dynamic range (i.e. having pixels range from 0 to 255 for 8bit images) and make it so that specific tissues of interest always assume the same average pixel intensity value.

Despeckling is also an important primary pre-processing step in ultrasound image analysis, but the application should be considered when attempting to find the most effective despeckle filter. The first order statistical filter has shown to provide the best results for despeckle filtering in carotid artery using ultrasound images [12]. Singh et al. [13], on the other hand, found that the best performing despeckle filter in breast ultrasound images is a wavelet filter. Other very useful techniques are speckle reducing anisotropic diffusion methods [14], [15], which are diffusion methods that encourage intra-region smoothing in preference to inter-region smoothing.

3. Automated organ/tissue localization and segmentation in ultrasound images

The main step in automatic ultrasound B-mode image analysis is the identification of the organ or tissue of interest, which at times also coincides with the final segmentation depending on the application. The ultrasound image always includes surrounding tissue or organs in the frame; occasionally the specific organ or tissue may present a very distinct morphology and characteristics as compared to the surrounding tissue, making the automatic detection a simpler phase. However, at times the organ or tissue of interest can present similar morphology and characteristics to the other surrounding tissue, but still can be automatically detectable with a priori anatomical knowledge (i.e., identification of the common carotid artery when the jugular vein is present in the ultrasound frame) [16].

When the final desired segmentation is too fine to be obtained starting from the entire ultrasound frame, a two-step segmentation process must be followed. An example application that requires a two-step segmentation process is vascular ultrasound imaging and the automatic measurement of the carotid artery intima-media thickness. First of all, a coarse localization of the entire tissue/organ must be done, which corresponds to roughly locating the carotid artery in the ultrasound frame in the example of vascular ultrasound imaging. This step can also be compared with the manual delineation of a specific region-of-interest (ROI) within the ultrasound frame, so as to limit the fine segmentation process in only a certain portion of the image. This is often the step that is manual in semi-automated segmentation techniques [17]–[20]. Once the ROI has been defined either automatically or manually, the second step is the employment of a fine segmentation technique to obtain the final segmentation and desired quantitative information. Considering the same example of vascular ultrasound imaging, the fine segmentation technique must automatically delineate the borders of the lumen-intima and media-adventitia borders so as to then calculate the distance between the borders, corresponding to the intima-media thickness.

Automated techniques for both the localization of organs and tissues and segmentation in ultrasound images can be divided into the following macro-areas, which are listed in no particular order of importance:

- Active Contours
- Shape priors
- Superpixel or patch-based and classification
- Texture and classification

- Pixel intensity and/or local statistics based
- Edge tracking
- Optimization techniques
- Transform-based
- Data-mining
- Heuristics
- Neural Networks and Deep Learning

It is important to note that while these techniques can be considered the mainstream segmentation methods that are available in literature, a combination of these methods are often employed in order to develop a specific algorithm for the desired application.

Active Contours

Active parametric contours can be either parametric, which also go under the name of *snakes*, or geometric, which are based on the level set method. Active contours (or deformable models) rely on the definition of internal and external energy and the evolution of an initial contour until the two energy functions reach a balance. Geometric deformable models can also be easily extended to 3D images. Both parametric and geometric deformable models require some sort of initialization which then evolves in time, so this segmentation technique can be considered as a fine-grain segmentation technique.

Active contours under the form of snakes have been employed widely in the second step of carotid ultrasound image fine segmentation and the subsequent calculation of the intima-media thickness. Considering this vascular application, an initial deformable model that is straight should be able to adapt to the carotid artery wall borders after the snake's parameters are properly tuned. Most studies adopt Williams and Shah's traditional formulation of a snake [21]. A 2D snake can be represented by $v(s) = [x(s), y(s)]$, where (x, y) represents the spatial coordinates of an image and $s \in [0, 1]$ denotes the parametric domain. The snake then evolves dynamically by reducing a global energy function:

$$E[v(s)] = E_{int}[v(s)] + E_{ext}[v(s)] \quad (3)$$

where:

- $E_{int}[v(s)]$ constrains the shape of the curve and is known as the "internal energy". This term is typically proportional to the curve derivatives so as to regularize the curvature and elasticity of the curve.
- $E_{ext}[v(s)]$ drives the curve towards the image intensity edges and is known as the "external energy". This term is often modeled by image gradients in some form.

A comprehensive study of carotid segmentation using snakes was done [22]. The same research team further improved their snake-based algorithm and made it completely automated [23] and suitable to process carotid arteries that present plaques [24].

A new approach to segmenting carotid ultrasound images with snakes was proposed by Molinari et al. in 2012 [25], [26]. Their approach consisted of a dual-snake system with two different active contours (for the two carotid wall borders, the lumen-intima and media-adventitia interface) evolving together. The energy functional that was defined for this snake $v(s)$ was:

$$E(v(s)) = \int_0^1 \alpha |v'(s)|^2 + \beta e(v(s)) + \gamma |v(s) - e(v(s))| ds \quad (4)$$

In this formulation, the first term represents the internal energy, $E_{int}(v(s)) = \int_0^1 \alpha |v'(s)|^2 ds$ where $v'(s)$ is the first-order derivative of the snake curve $v(s)$. The second and third terms, instead, represent the external energy: $E_{ext}(v(s)) = \int_0^1 \beta e(v(s)) + \gamma |v(s) - e(v(s))| ds$. In this formula, the functional $e(x, y)$ is an edge operator called FOAM (First Order Absolute Moment) [27], [28]. Since the FOAM operator, and therefore the first term of the external energy $\beta e(v(s))$, is equal to zero when the snake is found to be distant from edges, a second external energy term was added $\gamma |v(s) - e(v(s))|$. This energy term acts as an attraction term that brings the snake vertices closer when they are found to be distant from the actual boundaries. Another important and new feature of this dual snake was the introduction of a mutual constraint that compels the snakes to keep a specific constrained distance from each other, preventing the two active contours from collapsing onto or diverging from one another. **Figure 1** is an example of snake initialization and final segmentation.

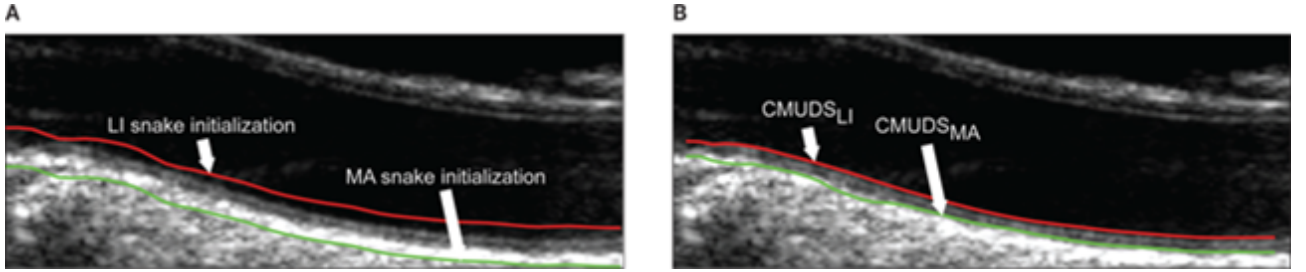


Figure 1. Example of active contour (snakes) initialization and segmentation. (A) Initialization of the lumen-intima (LI) and media-adventitia (MA) snakes. (B) Final segmentation after convergence (maximum 200 iterations). The MA snake moved by 1.8 mm, the LI snake moved by 1.5 mm. CMUDS = Carotid Measurement Using Dual Snakes (automatic algorithm). Figure taken with permission from [25].

As can be seen from the dual snake formulation, each snake has a total of three parameters that need to be optimized: α, β, γ . Parameter optimization represents a downfall for this segmentation technique, since (a) they must be fine-tuned in order to obtain an accurate segmentation, and (b) the parameters found to be optimal for one image database may have to be tweaked to work with images deriving from another database, if gain settings are very different and/or a different amount of noise is present.

Shape priors

Anatomical shape prior methods for ultrasound image segmentation are based on the fact that the expected anatomical structure is already known, offering a great advantage for segmenting them from the US images. These types of techniques can cope very well with suboptimal images, such as those with shadows and weak edges. They are also typically built from a large database of training samples to determine the final shape prior. On the other hand, however, this can present a major drawback, as the shape model can only be as good as the training samples and the chosen shape-space model framework. With this in mind, it should not be forgotten that pathology often presents itself as a variation in structure, shape, and size of lesions, making it challenging for the model to correctly adapt to the variety of pathologies that may be present. These methods are also often computationally expensive.

Depending on the application and implementation, this segmentation technique is quite versatile and can be used either to locate the tissue/organ of interest or to obtain the fine segmentation in two-step segmentation algorithms.

Ni et al. [29] recently demonstrated an improvement in the performance of active contour models by using shapes correlation in uterine fibroid images. The innovation in the proposed method is that while it uses shape prior to aid the final segmentation, no additional training samples are needed because the object shapes correlation is built as a patient-specific prior knowledge. In the method, active contours are used on every image individually to segment the borders. This technique showed consistent improvement compared to active contours without shape constraints in both synthetic and clinical images, but it should be underlined that this technique is only applicable with sequences of ultrasound images.

Superpixel or patch-based and classification

Superpixel or patch-based techniques for segmentation are mainly based on the division of the original image into superpixels or patches which are then labeled as belonging to either the object or background, using graph cuts. Dividing the image into superpixels can improve the robustness of segmentation methods to noise and reduce the complexity of the image from hundreds of thousands of pixels to only a few hundred superpixels.

This technique typically provides only a coarse segmentation which needs refining, so it is often used to determine the general area of the tissue/organ of interest in two-step segmentation algorithms.

An example of using this type of automatic segmentation technique can be found in the work by Wang et al. [30]. In this paper, the authors propose an automatic energy-based region growing method to automatically segment the lesion region in liver ultrasound images. After speckle reduction using the speckle reducing anisotropic diffusion method [14], a superpixels map was generated by using the simple linear iterative clustering algorithm [31] in order to segment the original input image into many (200 in this study) uniform and small compact regions. As a second step, the authors then implemented an automatic seed selection and energy-based region growing algorithm to obtain the final segmentation. The authors compared the proposed algorithm with manual segmentations and with the results obtained from four other popular segmentation techniques on 40 liver ultrasound images. The proposed algorithm was found to produce better segmentation accuracy than the other segmentation techniques.

Texture and classification

Texture and classification methods are based on finding the features of the microstructure of the tissue being imaged and consequently classifying the pixels or sections of the image into different regions based on these features [32]. A benefit of texture techniques is that they are typically based on pixel intensity statistical patterns, so they are more independent of the imaging system physics. Many of these texture techniques are based on the calculation of Haralick's co-occurrence matrices which, despite being computationally intensive, have performed favorably in various applications and studies [33]–[38].

This technique typically provides only a coarse segmentation which needs refining, so it is often used to determine the general area of the tissue/organ of interest in two-step segmentation algorithms.

Liu et al. [39] used local texture information to automatically generate ROIs that contain breast lesions in the ultrasound image. Instead of using the technique of modeling and classifying every single pixel that are present in earlier studies, such as the one by Boukerroui et al. [40], here the authors divided the image into

lattices of the same size and extracted the texture information of each lattice. In their study, the co-occurrence matrix was calculated and four texture descriptors (entropy, contrast, sum average, and sum entropy) were used in 4 directions (0°, 45°, 90° and 135°). Finally, the mean and variance of the intensities of each lattice were used as features, so a total of 18 features were extracted. To classify the lattices, the authors then employed a support vector machine (SVM) for classification. The ROI is then produced based on the outcome of classification and background knowledge-based rules.

Local statistics and/or pixel intensity

Pixel intensity and/or local statistics techniques rely on and exploit the specific appearance of the desired tissue in the ultrasound image. The object representation can be perceived as a mixture model with different intensity distributions, so the neighborhood of a pixel can be explored to determine whether it belongs to a certain structure/tissue or the background based on its intensity value, the mean intensity of its neighborhood and the neighborhood standard deviation. Segmentation techniques based on thresholding or region growing also fall within this category.

This segmentation method typically provides only a coarse segmentation which needs refining, so it is often used to determine the general area of the tissue/organ of interest in two-step segmentation algorithms. On the other hand, however, specific region growing techniques are often employed for fine segmentation in two-step strategies.

An example of this type of technique can be found in carotid artery ultrasound imaging, where (a) the pixels within the lumen region have an intensity value that is close to zero and a low neighborhood intensity standard deviation, (b) pixels of the carotid wall adventitial layer have a high intensity and a low neighborhood intensity standard deviation, and (c) the rest of the pixels have a different average intensity and a higher neighborhood intensity standard deviation. Molinari et al. [41]–[43] described such an approach in their works, where the authors considered a bi-dimensional histogram in order to mark all the pixels possibly corresponding to blood in the image. Then, the center of the lumen and the far adventitial wall can be easily marked by using simple conditions on the obtained mask. **Figure 2** illustrates the results using this strategy for the carotid artery localization in ultrasound images.

Another example of determining the lumen area in carotid artery ultrasound images is presented by Sifakis and Golemati [44]. The algorithm the authors proposed combines simple anatomical knowledge and statistics. Specifically, a statistics-based procedure using the local mean and variance is used on vertical intensity profiles (VIP) of the image to determine a single lumen center point. Then the lumen center points are further processed and refined to accurately estimate the location of the carotid artery lumen.

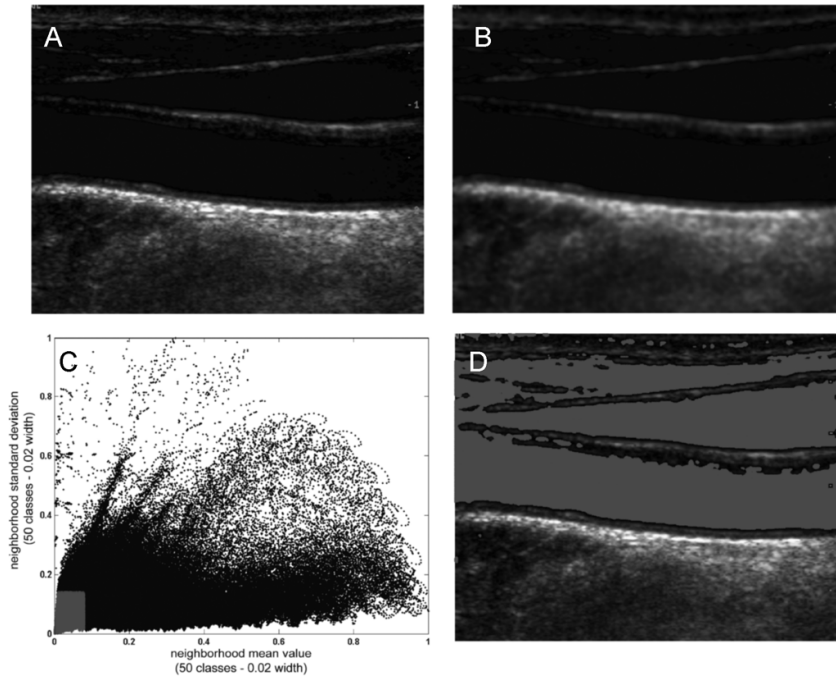


Figure 2. Strategy for localization of the carotid artery; tracing of the far wall adventitial layer. (a) Original image. (b) Bi-dimensional histogram (2DH). The gray portion of the 2DH highlights the locality in which it is supposed to only find lumen pixels. (c) Original image with lumen pixels overlaid in gray. (d) Typical processing of one column, showing the indicative points of the lumen and of the far adventitia layer. JV = jugular vein, CCA = common carotid artery. Figure taken with permission from [45].

Table 1. Summary of localization and segmentation techniques.

Type	Simple description	Advantages	Disadvantages	Coarse/fine segmentation	Examples
Active contours	Deformable model that evolves under the action of various forces	- considers both edge strength and shape together	- sensitive to parameter selection	Fine	[21]–[23], [25], [26], [46]–[54], [55]–[58]
Shape priors	Based on a priori knowledge of the expected anatomical structure	- robust to noise and artifacts	- computationally expensive - needs training set - sensitive to presence of pathology	Coarse Fine	[29], [59]–[65]
Superpixel and classification	Based on the division of the original image into superpixels and then classification into regions	- improved robustness to noise - reduction of complexity	- need to decide size of superpixel/patch	Coarse	[30], [61], [66], [67]
Texture and classification	Based on finding tissue microstructure features and then classification into regions	- more independent of physics of imaging system	- computationally expensive	Coarse	[39], [46], [68]–[70]
Local statistics/pixel intensity	Based on exploiting the specific appearance of the desired object in the ultrasound image	- simple implementation - not computationally expensive	- sensitive to noise and artifacts	Coarse Fine	[41]–[44], [65], [71]–[73]
Edge-tracking	Based on calculating the gradient or other edge detector of the image	- simple implementation	- sensitive to noise and artifacts - sensitive to orientation of boundary to transducer	Fine	[14], [15], [74]–[76]
Optimization techniques	Based on the search for the global optimum or best path by minimizing or maximizing specific functions	- reduces variability in ultrasound measurements - computational cost reduction	- need to correctly formulate function and parameters	Fine	[64], [74], [75], [77]–[79]
Transform-based/modeling	Based on modeling techniques or calculating specific mathematical transformations.	- considers shape - robust to noise and artifacts	- sensitive to presence of pathology - sensitive to the chosen model	Coarse Fine	[61], [80]–[92], [93]
Data-mining	Based on feature extraction, feature reduction/selection, classification, and boundary refinement	- analyzes much data and can find hidden and useful knowledge	- computationally expensive - sensitive to feature selection method	Coarse	[4], [94]–[96]
Heuristics	Based on heuristics when a search must be	- simple implementation	- sensitive to noise and artifacts	Coarse Fine	[97], [98]

Neural Networks and Deep Learning	done along, for example, the entire width of the image		- requires knowledge and experience	
	Based on the training and learning of the computer without explicit programming	- ability to learn without handcrafted features - numerous layers that can capture different patterns	- computationally expensive - requires large amount of training data - results depend on training data size	[99][66] Coarse Fine

Edge-tracking and gradient-based

Edge tracking and gradient-based techniques for ultrasound segmentation are appropriate if the aim is to locate acoustic disruptions. This type of method, however, assumes stable intensity on both sides of the boundary and suffers from image acquisition anisotropy, since the edge strength in an ultrasound image depends on the relative orientation of the probe to the border. Moreover, two other potential problems of these techniques are that deeper objects have weaker edges because of greater signal attenuation, and speckle produces an intensity gradient response that is quite strong. To overcome these problems, speckle reducing anisotropic diffusion (SRAD) methods are often employed [14], [15].

Due to these challenges with edge-tracking in ultrasound images, these segmentation techniques are often used only once a specific ROI has been determined, so as a second fine segmentation algorithm in two-step methods in order to reduce the number of plausible edges that make up the desired object.

An example of a SRAD method for ultrasound image edge detection is provided by Yu and Acton [14], [15], using the Instantaneous Coefficient of Variation (ICOV). The ICOV is based on normalized gradient and Laplacian operators. Considering the image intensity at a certain position (i, j) as $I_{i,j}$, the instantaneous coefficient of variation $q_{i,j}$ is given by:

$$q_{i,j} = \sqrt{\frac{\left| \left(\frac{1}{2} \right) \|\nabla I_{i,j}\|^2 - \left(\frac{1}{16} \right) (\nabla^2 I_{i,j})^2 \right|}{\left(I_{i,j} + \left(\frac{1}{4} \right) \nabla^2 I_{i,j} \right)^2}} \quad (1)$$

where ∇ , ∇^2 , $\|\cdot\|$, and $|\cdot|$ are the gradient, Laplacian, gradient magnitude, and absolute value, respectively. Specifically, $\|\nabla I_{i,j}\|^2 = 0.5 \left[\|\nabla_- I_{i,j}\|^2 + \|\nabla_+ I_{i,j}\|^2 \right]$ where $\nabla_- I_{i,j} = [I_{i,j} - I_{i-1,j}, I_{i,j} - I_{i,j-1}]$, $\nabla_+ I_{i,j} = [I_{i+1,j} - I_{i,j}, I_{i,j+1} - I_{i,j}]$; and $\nabla^2 I_{i,j} = I_{i+1,j} + I_{i-1,j} + I_{i,j+1} + I_{i,j-1} + 4I_{i,j}$.

From this definition, it can be seen how homogeneous regions of the ultrasound image should present low ICOV values, while boundaries will have large ICOV values, appearing as outliers. This operator also allows for edge detection in dark and bright regions. Figure 3 shows a few examples of ultrasound images and their resulting ICOV edge strength images.

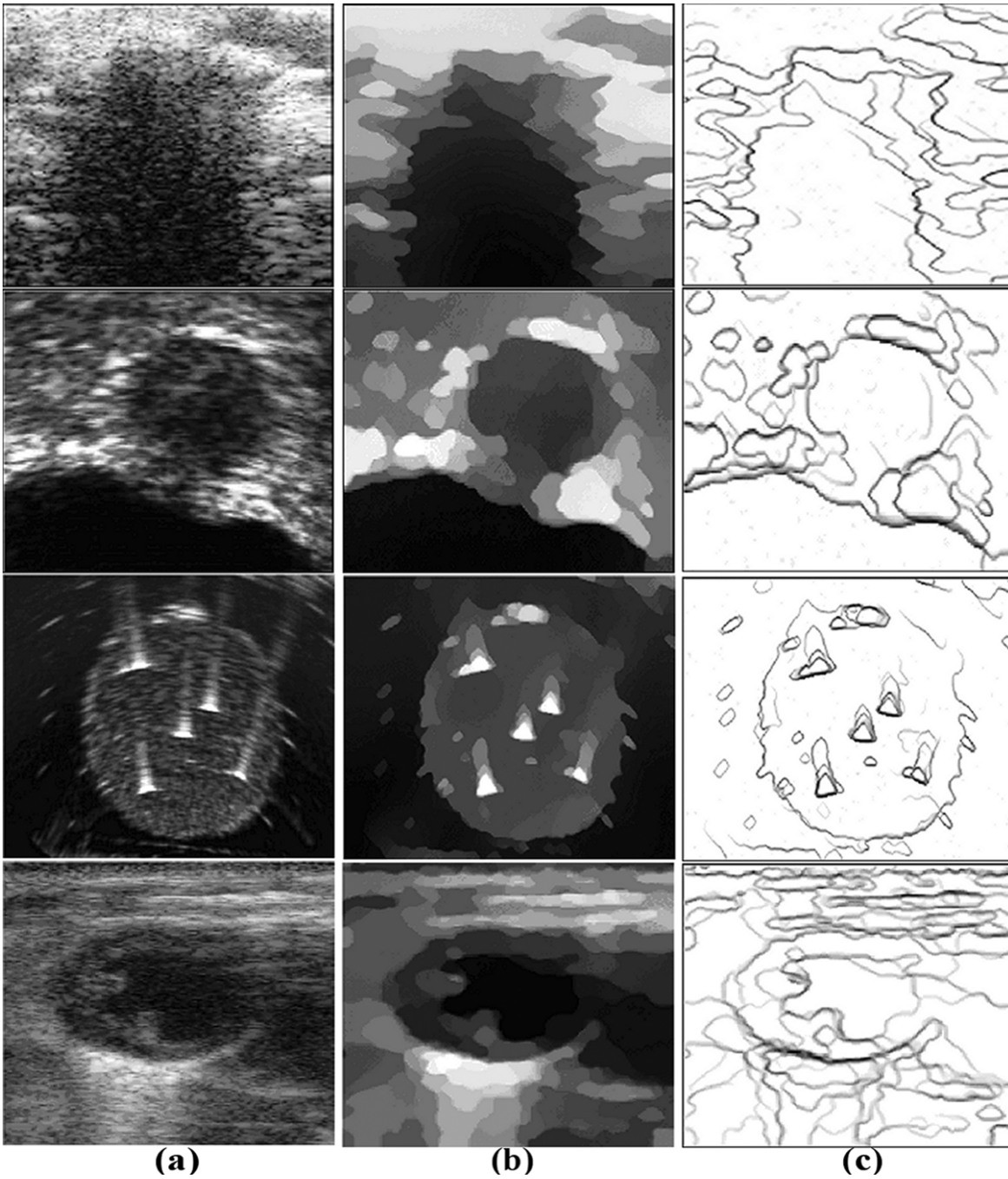


Figure 3. Experimental results of the ICOV-based edge detection method using four B-mode US images. First column, from top to bottom: ultrasound images of a human throat, a human prostate, a prostate phantom with implanted radioactive seeds, and the left ventricle of a murine heart, respectively. Second column: Diffused images. Third column: ICOV edge-strength images. Figure taken with permission from [15]].

Optimization techniques

Optimization techniques are used to search for the best path or the global optimum by either minimizing or maximizing a specific cost function or other specific functions. Dynamic programming is a commonly used optimization method that was first developed in the early 90's to lower the variability in ultrasound measurements [100] and to help minimize the computational cost of algorithms by not needing to inspect

all points of the image. Dynamic programming was first used for automated identification of echo interfaces by Wendelhag *et al.* [101].

Based on the application, this type of segmentation algorithm is often used only once a specific ROI has been determined, so as a second fine segmentation algorithm in two-step methods.

Timp and Karssemeijer [78] introduced a 2D dynamic programming method for the segmentation of masses in breast ultrasonography. Their technique relied on the manual insertion of one point in the center of the mass, after which a circular ROI large enough to contain suspect lesions was automatically generated. In their study, the local cost components formed the following cost function:

$$c(i, j) = w_s s(i, j) + w_d d(i, j) + w_g g(i, j) \quad (2)$$

where s denotes the edge strength, d and g are the deviation from an expected size, and gray level respectively. Also, w_s, w_d, w_g are the weights for the components.

Transform-based and modeling

Other methods that accurately segment objects in ultrasound images rely on modeling techniques or mathematical transformations.

A commonly used transformation approach is the Hough transform [80] which enables an efficient detection of specific shapes in an image. This transform is typically employed to detect (a) lines, such as the carotid artery borders [81] or muscle fascicles [82] and (b) circles, such as thyroid nodules [83] or the fetal cerebellum in 3D ultrasound volumes [102]. Another common transform used in image segmentation is the watershed transform.

Based on the application, these types of segmentation algorithms can be employed both to locate the final tissue/organ of interest within the entire ultrasound frame or within a specific ROI as the second step in two step segmentation algorithms.

A hybrid multi-scale model was employed using the Hough transform for thyroid nodule boundary detection in the study by Tsantis *et al.* [84]. Their proposed technique involved three main steps. Speckle reduction and edge map estimation was first done using wavelet edge detection. Then a contour representation was obtained from a multiscale structure model using local maxima. Finally, the constrained Hough transform was used to discriminate it from its neighboring structures thanks to the a priori knowledge of the nodule's circular shape. **Figure 4** shows the summary of this technique and final delineated boundary.

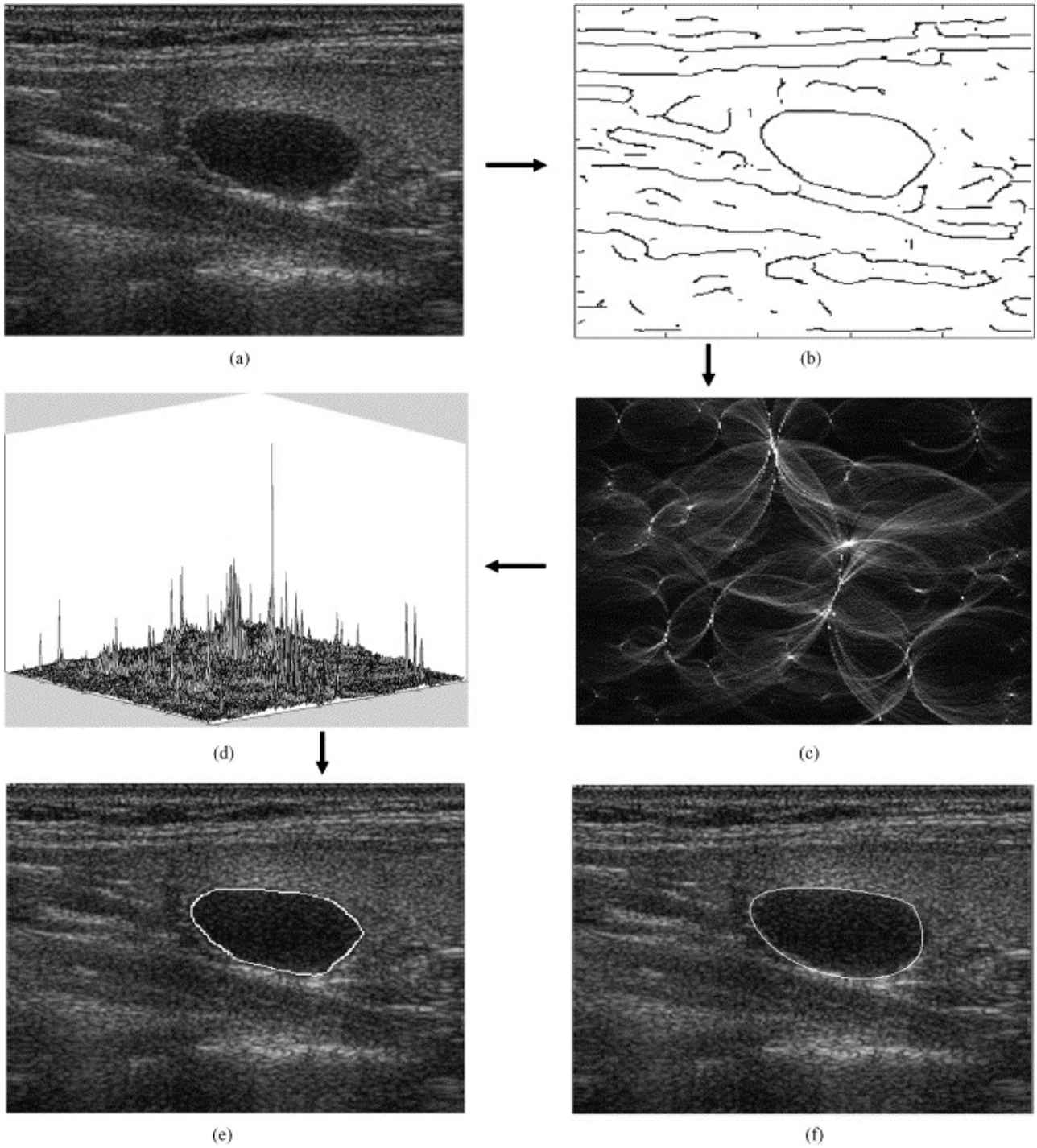


Figure 4. Example of Hough transform and automatic thyroid segmentation. (A) Ultrasound image with a hypoechoic thyroid nodule, (B) contour representation, (C) constrained Hough transform, (D) accumulator array, (E) hybrid model outcome, and (F) manually traced boundary. Figure taken with permission from [83].

As far as modeling approaches go, the image is considered as the combination of the intensity of the desired object plus noise. Taking vascular ultrasound imaging as an example, an image region containing a portion of the vessel lumen, the wall, and some surrounding tissues could be characterized by the specific distributions mimicking the intensity distributions of the three components. An example that has been extensively used for US image segmentation is the Markov random field (MRF) model [103]–[105]. The MRF

tries to identify regions of similar intensity inhomogeneity, and alternatively approximates the maximization of the posterior estimation of the class labels, and estimates the class parameters. Many other modeling techniques require the RF lines of the ultrasound image and not the B-mode beamformed image, so in this work we will not go into detail about these RF methods. It is important, however, for the reader to be aware that these techniques exist and that there are many model distributions such as the Weibull, normal and log-normal and gamma [106], Rayleigh, Nakagami, Rice, inverse Gaussian, and K-distribution [60], [107].

Data mining

These techniques have recently been applied to ultrasound image segmentation thanks to the growing interest in data mining and big data. The majority of these methods follow the same general pipeline: (1) feature extraction, (2) feature reduction/selection, (3) classification, and finally (4) boundary refinement.

As the pipeline suggests, the actual results from data mining algorithms typically provide results that need refining, so this type of segmentation technique can be used as a way to locate the initial organ/tissue of interest or also within a specific ROI to provide an initial segmentation that is then refined.

Cheng et al. [4] provided a comprehensive review on automated breast cancer detection with ultrasound images. In their work, features of breast US images are separated into four groups: descriptor, model-based, morphologic, and texture features. First of all, various image features are extracted from the image (step 1). Since there are many different features available, there is the risk of having collinear variables that could lead to an over-constrained system. So, a mandatory task is to find the optimal set of features with relative low dimensions. Collinear and strongly correlated variables are taken out, whereas variables with negligible variance are ignored. To do so, either feature extraction (i.e., principal component analysis) or feature selection (i.e., linear stepwise feature selection) is employed (step 2). Rosati et al. [94] also recently revised the most performing and widely used feature reduction and selection techniques for vascular ultrasound images. Once the features have been extracted and selected, a classification process must occur to categorize the pixels of the image into specific image components (step 3). Pixels with borderline conditions are typically kept in an “uncertainty” class and ignored. Common classifiers are: linear classifiers, fuzzy classifiers and neural networks (Bayesian, artificial, back-propagation). Finally, the boundaries obtained from the classification process are usually not accurate enough to be considered as the final segmentation, so a boundary refinement process is typically done (step 4).

Heuristics

Heuristic functions, also called heuristics, are a type of segmentation method that ranks alternatives in search algorithms at every branching step based on the available information in order to decide which branch to follow.

These kinds of techniques are employed when the same sort of search must be done along, for example, the entire width of the image. In this way, a heuristic search examines each column of the image using the same rules to detect the desired tissue. Depending on the application, the heuristic search can be either employed along the entire original ultrasound frame or within a specific ROI that contains the object of interest.

An example of a heuristic search used for segmentation can be found in the muscle ultrasound analysis (MUSA) algorithm proposed by Caresio et al. [98]. In this automated algorithm, a binary FODG (First Order

Derivative Gaussian) mask is first obtained to find all possible aponeuroses candidates. Once potential fascicles and very small candidates are removed from the mask, the image is considered column-wise and the candidates are considered starting from the deepest. First of all, the deepest candidate and the closest candidate upwards are found and a ROI is determined. If the height of the ROI is found to be too small, the closest candidate found previously is discarded and the next closest candidate is determined. Then, once this condition is fulfilled, the two candidates are segmented as the final deep and superficial aponeurosis only if a large enough number of muscle fascicles is found between them. If this condition is not met, then the deep aponeuroses candidate is discarded and the process starts again. **Figure 5** illustrates this process.

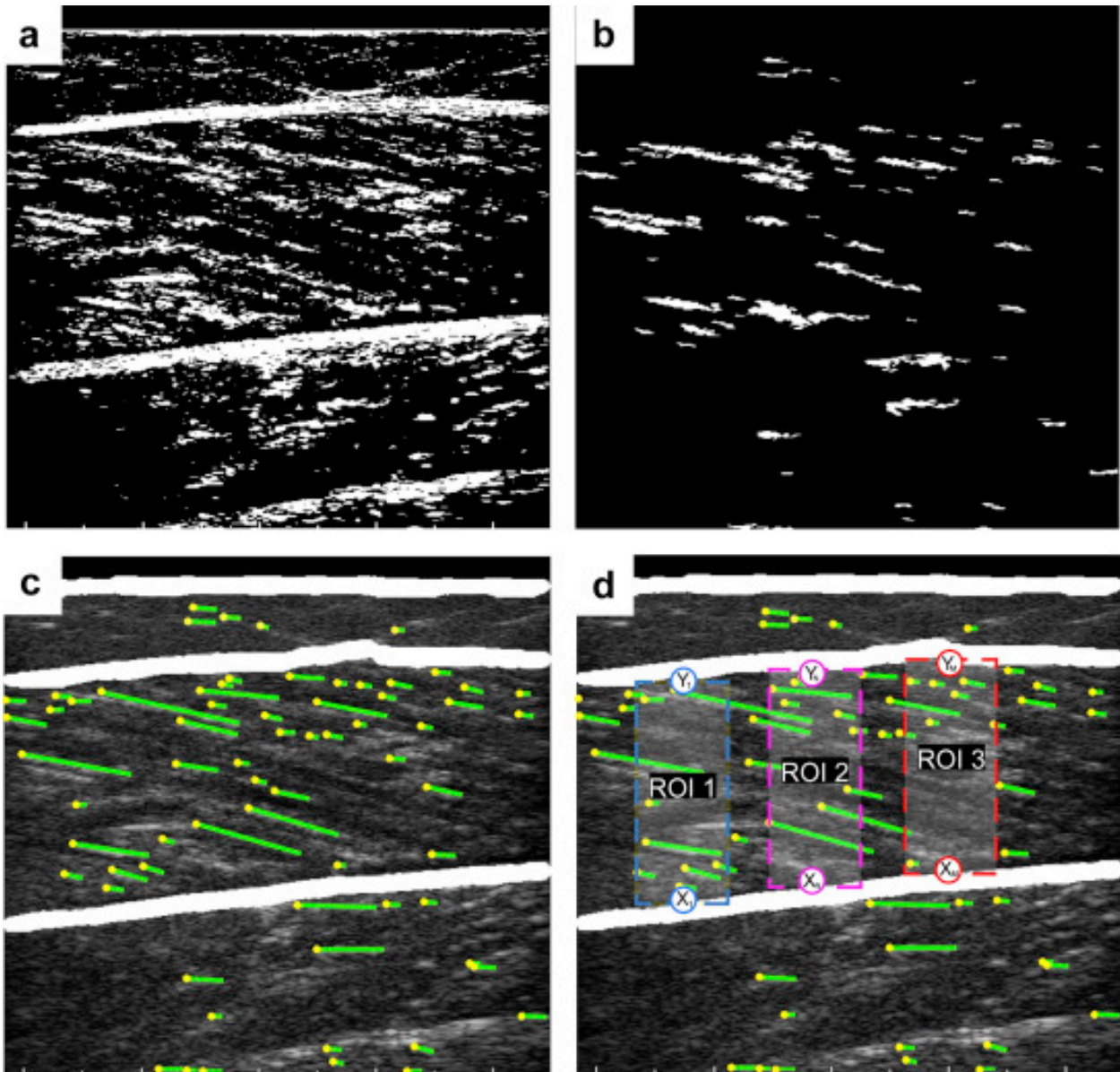


Figure 5. Heuristic strategy for segmentation of muscle aponeuroses. (a) Binary mask obtained with image equalization and Otsu thresholding; (b) cleaned fascicle mask; (c) Final fascicles mask overlaid on original image. The fascicles are portrayed in green, whereas the endpoints of the fascicles are in yellow; (d) sketch of the heuristic search. The fascicles are shown in green, the endpoints in yellow and three example ROIs are drawn in dotted rectangles. Figure taken with permission from [98].

Neural networks (NNs) and deep learning is a technique used for implementing machine learning, the science of having computers act without being directly programmed, and is an advancement of data mining techniques [108]–[111]. Deep learning, or a deep neural network, allows multiple processing layer computational models to learn representations of data with multiple levels of abstraction [109], [112]–[114]. NNs can learn a hierarchical representation of input data without requiring the design of handcrafted features, but do require a large amount of training images in order to correctly learn the network parameters. If there is a higher amount of training data available, it is possible to see a significant performance increase [115]. NNs can be either employed using the entire original ultrasound frame or within a specific ROI that contains the object of interest, so they can be applied both as a coarse or fine segmentation technique.

Milletari et al. [116] proposed an approach to segment transcranial ultrasound volumes using convolutional neural networks (CNNs). Their approach used CNN classification outcomes along with voting by exploiting the features obtained by the deepest section of the network, and they studied the impact of the amount of training data and the data dimensionality using six different architectures. The proposed method outperformed voxel-wise semantic segmentation of CNNs with all of the different parameters settings and found a best Dice similarity coefficient (DSC) to be equal to 0.85 with 0% failures.

5. Selected applications

In this section, we will discuss semi-automated or automated segmentation algorithms of ultrasound images in abdomen/kidney, breast, cardiology, thyroid, liver, vascular, musculoskeletal, obstetrics, gynecology, and prostate.

1. Abdomen/Kidney

Ultrasound imaging is commonly used for kidney analysis, and specifically for renal calculi diagnosis, kidney cyst or tumor detection, and measurement of kidney size. During the ultrasound scan, kidneys appear either as a football shaped or a C-shaped structure, depending on whether it is scanned in a longitudinal or transverse view, respectively. Normally the kidney presents a more hyperechoic region around it, which consists of perinephric fat and Gerota's fascia [92]. The peripheral zone typically appears grainy gray, and consists of the renal cortex and pyramids, whereas the kidney's central area, the renal sinus, appears brighter. Figure 6 shows some sample images for abdomen and kidney ultrasound images.

The automatic segmentation of the entire kidney is necessary for accurate kidney morphology measurements, which can help discriminate between chronic and acute kidney failure and is also useful in determining hydronephrosis in children [117]. Kidney segmentation is challenging due to the fact that the kidney shape and size is very variable, and that there is a weak contrast of the actual kidney boundaries, whereas there are often strong edges at the diaphragm and fat layers [118].

Due to these challenges, kidney segmentation techniques almost always rely on some sort of shape prior or model, both considering 2D and 3D kidney images [119]. Much focus is also given to texture analysis, which can help overcome some of these challenges as well. Older techniques often require some kind of user interaction, by manually placing markers to delineate in some way the initial segmenting curve or model [46], [59], whereas more recent research has focused on completely automatic techniques on 3D ultrasound images, often integrating ad-hoc or patient-

specific functions [57], [58], [117], as personalized medicine is becoming a main focus in medical imaging.

To note are the completely automatic kidney segmentation techniques from 3D US images developed by Cerrolaza et al. [117], based on fuzzy appearance models and patient-specific alpha shapes that allows to control an ad-hoc stopping function created from the adipose tissue bands within the kidney, and by Marsousi et al. [58], who developed a technique that offers a new shape model representation that combines anatomical knowledge with prior knowledge of training shapes. The first method by Cerrolaza et al. tested the algorithm on a dataset of 39 cases, showing an average Dice similarity coefficient equal to 0.86 ± 0.05 ; the method proposed by Marsousi et al. instead showed a Dice similarity coefficient of 0.81 ± 0.04 on a database of 46 ultrasound volumes. The second study also included an important inter-operator variability analysis, showing a DSC agreement equal to 0.83, and a comparison with other state of the art methodologies (deformable model, fast marching method and level set [55] with $DSC = 0.57 \pm 0.08$; shape prior based on manual segmentations and level set [56] with $DSC = 0.42 \pm 0.08$).

Going more into detail and segmenting lesions within the kidney or other abdomen organs, tumor segmentation has not been a main focus in B-mode ultrasound kidney imaging. In fact, research has mainly focused here on contrast-enhanced ultrasound imaging for the characterization of kidney lesions [119] and on the direct classification of kidney lesions [120], [121]. Still, Li et al. [122] compared the performance of five categories of techniques for kidney tumor segmentation: (1) Edge or boundary based, (2) Region based, (3) Texture based, (4) Active contours, and (5) Model based [123]–[127]. The algorithms were tested, however, on a very small database consisting of forty phantom images and only one in-vivo patient kidney cyst image. In any case, the results showed a comparable Dice similarity coefficient greater than 0.94 for all techniques for the phantom data. For the in-vivo kidney cyst image, on the other hand, the texture-based segmentation showed the best results with $DSC = 0.91$. Edge-based and Region growing algorithms presented good results with $DSC = 0.89$, whereas the MRF model-based and active contour-based algorithms showed acceptable results with a DSC equal to 0.87 and 0.83, respectively.

Another focus in kidney and abdomen ultrasound imaging is in the automatic detection of renal calculi, which typically are present in the ultrasound image as hyperechoic structures with acoustic shadowing. The proper segmentation and localization of renal calculi is clinically extremely important for monitoring and following the kidney stone in extracorporeal shock wave lithotripsy [128]. While not an extremely hot topic in ultrasound segmentation research, different types of techniques are present in literature, varying from techniques based on the watershed transform [93], entropy analysis [129], and seeded region growing based on texture features [130].

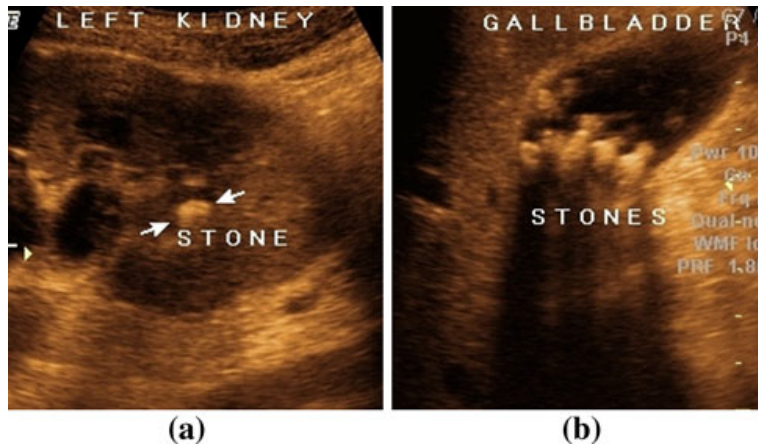


Figure 6. Abdominal ultrasound sample images containing stones. (A) Kidney stone (B) Gallstones. Taken with permission from [93].

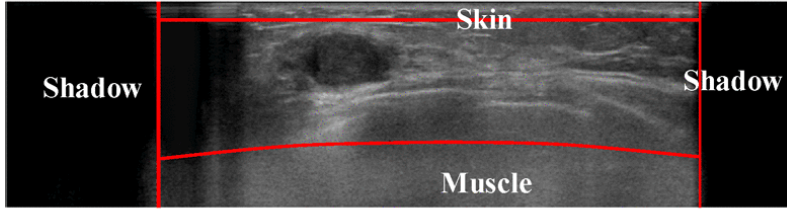
2. Breast

Ultrasound imaging is currently employed to observe and diagnose abnormalities in the breast. Studies have shown that ultrasound can identify and distinguish benign and malignant masses accurately and minimize the number of unnecessary biopsies [131]–[134]. Breast tumors typically appear as a hypoechoic structure in the ultrasound image, with a more or less circular form. The presence of various ultrasound artifacts, such as high speckle presence, blurry boundaries, low signal-to-noise ratio, low contrast, and intensity inhomogeneity make this segmentation process not an easy task. Due to this, the principal segmentation techniques focus on the characterization of the lesion's textured appearance and geometry as compared to normal tissue and typically incorporate various higher-level segmentation techniques.

Figure 7 shows an example breast ultrasound image and preliminary results of a segmentation technique that will be discussed in the following paragraphs.



(a)



(b)



(c)



(d)

Figure 7. Example breast ultrasound image and abnormality extraction. (A) Ultrasound image with circled tumor. (B) Illustration of skin, muscle, and shadows in the image. (C) Result after applying watershed transform. (D) Extracted suspicious abnormalities. Figure taken with permission from [135].

Much research has also focused not only on the segmentation of the breast tumor but on the feature extraction and subsequent classification of the tumor, which is outside of the scope of this paper. For more information on this subject, refer to the survey of automated breast cancer identification and classification in ultrasound images done by Cheng et al. [4].

Recently, Huang et al. [136] published a survey on breast ultrasound image segmentation, focusing on techniques adopted over the last 10 years. In this study, segmentation techniques were divided into seven classes, based on: thresholding, clustering, watershed, graphs, active contour models, Markov random fields, and neural networks. As the comparison found in Huang et al.'s study, the three completely automatic best performing algorithms in terms of True Positives (TP) of the segmentation lesion were those based on neural networks [137] with TP = 92.8%, clustering [138] with TP = 92.4% and Markov random fields [104] with TP = 90.1%. Many of the algorithms that were compared were also only semi-automatic, requiring some user interaction to obtain the final

segmentation. For more details and comparison, the readers are redirected to the complete study [136].

A new point of research is the analysis of B-mode ultrasound volumes coming from automated whole breast US (ABUS) scans. Automatically imaging the entire breast volume produces ultrasound images that are not as operator dependent and have a better reproducibility for follow-up studies [135]. Having an entire volume of images to analyze makes the automated processing of the images an even more critical aspect, since it can accelerate the review process and reduce oversight errors [139]–[143].

The majority of segmentation techniques for ABUS lesions are based on the extraction of image features, such as topological texture features [70] or voxel-specific morphology, intensity and texture features [135], [144], and then the subsequent classification of voxels as breast mass or normal tissue (Figure 7). The fact of combining numerous image features to classify voxels often overcomes artifact issues that are present in ABUS images, but at the same time increases the computational complexity of the algorithms which are not real-time and could therefore not be as practical for clinical use. Another disadvantage of these types of techniques is that they generally focus on the segmentation of the most common presentation of invasive carcinomas (i.e., with hypoechoic properties). Therefore, tumors that present little mass, such as lobular carcinoma, or tumors that are hyper/iso-echoic, such as mucinous or colloid carcinomas are overlooked and not segmented correctly with the algorithms.

A method worthy to note here is a technique presented by Ye et al. [70] which along with extracting texture features, also included 3D region-based features and multi-view information through the application of a 3D geodesic active contour framework. This implementation includes more anatomical and multi-view information when compared to other techniques found in literature, and provided good final results, which can be seen in Table 2 along with validation results of other ABUS segmentation techniques.

A performance measure that is often used with ABUS segmentation techniques is the sensitivity of tumor detection obtained guaranteeing a certain number of false positives (FP). As Table 2 shows, the algorithm presented by Ye et al. [70] based on topological texture features and a geodesic active contour presented the best results of sensitivity with the lowest rate of FPs, 70% at 1.6 FPs per volume. The technique by Lo et al. [135] was able to obtain a sensitivity of 100% but had a higher FP per volume rate, going up to 9.44.

Table 2. Validation of ABUS segmentation methods

Reference	Year	Segmentation method	Database size	Performance	
				Measure (Metric)	Value
Tan et al. [144] [95]	2013	Voxel feature extraction, likelihood map local maxima extraction, region segmentation and classification	169 volumes (malignant)	Sensitivity (FROC analysis)	70% (FPs/volume=2)
			154 volumes (benign)		64% (FPs/volume=1)

Lo et al. [135]	2014	Topographic Watershed and image feature false positive reduction	65 volumes (malignant)	Sensitivity (False positive (FP) reduction)	100%
					(FPs/pass=9.44)
					90%
					(FPs/pass=5.42)
					80%
Ye et al. [70]	2014	Topological texture features (Minkowski) and geodesic active contour	68 volume (benign)	Figure of Merit	(FPs/pass=3.33)
					0.46
					95%
					(FPs/volume=4.3)
					90%
Ye et al. [70]	2014	Topological texture features (Minkowski) and geodesic active contour	51 volumes	Sensitivity (False positive (FP) reduction)	(FPs/volume=3.8)
					70%
					(FPs/volume=1.6)
					Detection rate
					95%

Along with actual breast tumor segmentation in ABUS images, a few research groups have also focused on the automatic chest wall segmentation in 3D breast ultrasound scans, so as to be able to automatically remove identified cancer candidates beyond the chest wall, and to permit an easier intra- and inter-modal image registration process [86].

3. Cardiology

Cardiac imaging mainly involves segmentation and registration methods which are widely used to evaluate heart functionality [3], [145]. The segmentation of the heart within the ultrasound image provides structural information and registration methods typically evaluate the local functional analysis which aids in the treatment and diagnosis of patients. Recent research has focused largely on 3D cardiac modeling techniques and segmentation [145]–[147].

Cardiac segmentation involves the delineation of the epicardium and endocardium of ventricles and atria. The epicardial segmentation is typically more challenging due to poor contrast and the similarity of the tissue of interest and its surroundings. The endocardial border instead presents a good contrast between blood and the myocardium. However, the presence of the papillary muscles creates an extra challenge in automatic cardiac segmentation, since they are considered as part of the blood pool and should be avoided in the segmentation process [3].

The majority of segmentation techniques have focused on the segmentation of the left ventricle, but the right ventricle's role in cardiovascular diseases has been gaining more recognition over the last 10 years, making the segmentation of the right ventricle of more and more clinical interest [148], [149]. **Figure 8** shows an illustration and example ultrasound image of the apical long-axis view of the heart.

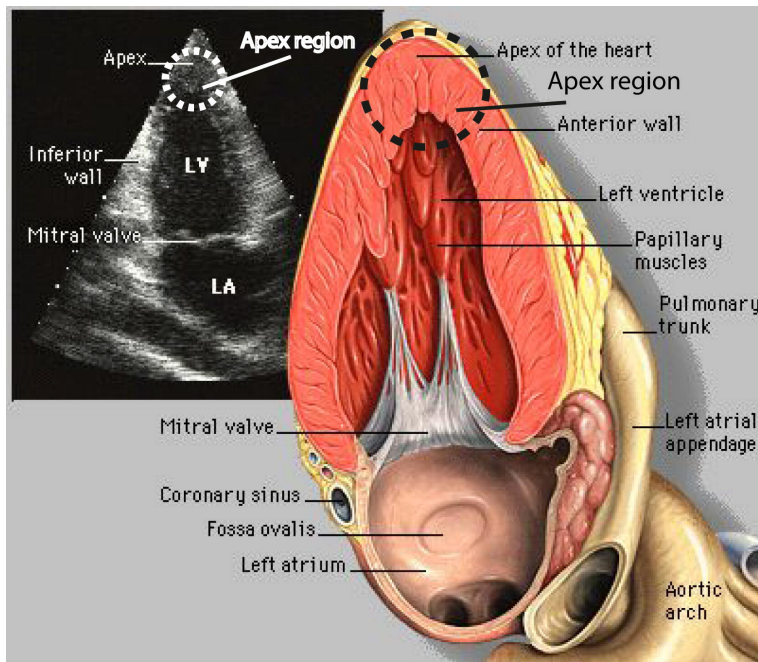


Figure 8. Two-chamber apical long-axis view of the human heart. Figure taken with permission from [60].

Noble and Boukerroui [3] presented a comprehensive overview of cardiac ultrasound imaging techniques until 2006 [39], [141]–[147]. Recently, Tavakoli and Amini [145] also presented a review on various segmentation and registration techniques applied to cardiac images.

The focus here in these next few paragraphs will be on recent advances and specifically 3D or temporal segmentation techniques.

The majority of 3D segmentation strategies are either based on pixel value regions or deformable models and shape priors, with a high tendency towards the employment of active contours. There are also a few biophysical/mechanical models that can be used as constraints for segmentation and motion estimation of cardiac ultrasound images, specifically isotropic cardiac mechanic models which consider the heart as a homogeneous medium and the incompressibility of the myocardium during systole and diastole [145], [157]. The segmentation techniques based on active contours or some sort of motion model often also incorporate some sort of shape constraint that must be identified by manual segmentations or assuming a specific geometry. This introduces a learning phase in the segmentation process that could require adjustments when images from other datasets or of different pathologies are analyzed. Moreover, as the complexity of the algorithm increases, the computational cost of the technique also increases, often times providing perhaps more accurate results but requiring much longer processing times.

To note here are two different methods, both including some advantageous points when compared to other methods found in literature. First of all, Barbosa et al. [49] developed a novel 3D level set method depending on the global intensity within and outside the object borders. Importantly, this method was also based on an additional local regional intensity term and on limiting the topology and shape of the interface. This technique had a very low computational cost, making it applicable for analysis of 4D ultrasound data as well (i.e., 3D volumes over time), but in this study the algorithm was tested on a very limited dataset. Secondly, Hansson et al. [60] proposed a new Bayesian formulation that incorporated priors for preferred shapes and position,

including also spatial and temporal smoothness. A novel addition in this group's work is the application of a censored gamma mixture model that is robust to artifacts. The method does not produce just a final segmentation but highlights uncertain areas and suggests possible segmentations for the operator. The authors tested the algorithm on a larger dataset (28 ultrasound videos) but required some user-interaction and was also computationally expensive (total running time = 2.5h).

4. Thyroid

The thyroid gland is a butterfly-shaped organ composed of two cone-like lobes. This gland controls the secretion of the thyroid hormone, whose intensity fluctuation causes pathological changes in the thyroid (too large or too small). For this reason, physicians often diagnose abnormal thyroid gland symptoms by its volume [66]. The presence of echo perturbations and speckle throughout the image make the segmentation of the thyroid more challenging, but in a longitudinal US image, the thyroid is also always contained between a bright strip and a dark area, which facilitates the coarse localization of the organ.

Similarly, ultrasound imaging is also employed for the diagnosis of thyroid nodules. Thyroid nodules are generally characterized as hypo-, iso-, or hyperechoic. Hypoechogenicity is generally associated with thyroid malignancy [158], however most thyroid nodules are heterogeneous with various internal components, which makes the automatic segmentation of nodules not an easy task.

Figure 4 shows an example of a thyroid ultrasound image.

Thyroid volume

The thyroid volume can be estimated by taking 2D ultrasound images of each lobe and multiplying its dimensions $length_{max}$, $width_{max}$ and $depth_{max}$ and a correction factor, f (typically 0.5 in clinical routine) or by using 3D ultrasound images for a direct volume measurement. As far as thyroid volume estimation segmentation algorithms are concerned, techniques found in literature are typically deformable model-based or pixel classification/machine learning-based [66].

A few papers comparing 2D ultrasound thyroid segmentation methods have been published, showing that an improved normalized graph cut [159] or a localized region-based active contour algorithm [160] provided satisfying results when compared to other basic segmentation techniques. However, little information about the testing procedure for both studies is provided.

Regarding 3D thyroid segmentation techniques, Wunderling et al. [159] recently published a comparison between three basic segmentation algorithms on healthy patients: active contours (level set), graph cuts and feature classification. All three techniques required a various amount of user interaction for initialization, however, and the volume was segmented by independently segmenting each 2D slice. A main point of this study was how future work will focus on combining the segmentation methods to improve accuracy.

Thyroid nodule detection

Recent studies have shown that the 3D ultrasound analysis of thyroid nodules has a higher sensitivity than 2D in predicting malignancy [160], [161], but 3D segmentation techniques for thyroid ultrasound images have up to now focused mainly on thyroid volume and not nodules. Here we will therefore analyze 2D segmentation techniques, whose validation results can be seen in Table 3.

The variability of thyroid nodule appearance in ultrasound images makes automatic segmentation quite difficult, and the US images are often affected by intensity inhomogeneity and weak edge borders of the nodules, often creating the problem of boundary leakage into adjoining tissue. The majority of techniques for thyroid nodule segmentation are based on level sets or feature selection and classification.

Active contour models typically show a low evolution efficiency and by themselves are not capable of accurately segmenting the weak edges of thyroid nodules, so they have often been used in combination with some other technique either for an accurate rough initialization or to control the evolution of the model, such as fuzzy C-means [162], neutrosophic L-means [163], adaptive diffusion flow [164], or joint echogenicity- texture [165]. The majority of these techniques, however, tend to deal with thyroid nodules that all present the same general appearance in ultrasound images, typically hypoechoic nodules.

A method that distinguishes itself in this area is the one proposed by Savelonas et al. [165], based on active contours guided by both texture and echogenicity. This technique integrates statistical texture information encoded by feature distributions along with regional image intensity and was also completely automatic thanks to an automatic ROI estimation [97]. In this study, the authors confronted both lesions that were hypoechoic as well as those that were isoechoic, showing a good performance for both.

As can be seen by Table 3, it can be difficult to make a direct comparison between thyroid nodule segmentation techniques since different performance metrics are used, while still portraying in some way the accuracy of the segmentation. The accuracy can be calculated by measured the mean absolute distance between the manual and automatic border, by calculating the overlap between the area of the two segmentations, or by simply calculating the percentage of nodules segmented and classified correctly.

Table 3. Validation of ultrasound thyroid nodule segmentation methods

Reference	Year	Segmentation method	Database size	Performance	
				Measure	Value
Tsantis et al. [83]	2006	Wavelet transform and Hough transform	40	Accuracy (percentage mean absolute distance)	90% (operator 1) 89% (operator 2)
Savelonas et al. [165]	2009	Joint echogenicity- texture (JET) active contour	74	Accuracy (Overlap)	91 ± 4 %
Legakis et al. [51]	2011	Texture and shape, active contours	142	Accuracy (Overlap)	92 ± 4%
Bibicu et al. [95]	2012	Feature selection and pixel classification	40	Accuracy (% correctly classified)	83% (whole image) 91% (ROI)

Chang et al. [164]	2016	Adaptive diffusion flow for active contours	118	Accuracy (% correctly classified)	84.7%
Xin and Wen- Jie [162]	2016	Kernel fuzzy c- means and distance regularized level set evolution (DRLSE)	4	Dice similarity coefficient	96.6 ± 1.1%
Koundal et al. [163]	2017	Neutrosophic-based distance regularized level set (NDRLS)	138	Dice similarity coefficient	93.8 ± 3.14%

5. Liver

In the ultrasound scan, livers typically appear as a structure with average echogenicity and a homogeneous texture, and ultrasound imaging is commonly used in diagnosing focal liver lesions (FLLs). A typical cyst in the liver appears as a thin walled anechoic lesion with posterior acoustic enhancement; a typical hemangioma (HEM), the most common primary benign FLL, instead appears with a well circumscribed uniformly hyperechoic area; finally a typical metastasis (MET) presents a “target” or “bull’s-eye” appearance, with a hyperechoic rim and hypoechoic center (Figure 9) [166].

Research has also focused on distinguishing normal liver from fatty liver disease, but the majority of these techniques are based on texture analysis of the entire ultrasound image, precluding a segmentation phase, so these methods will not be analyzed here [167].

The variability of lesions and their respective appearance makes automatic segmentation a challenging task. The majority of segmentation methods present in literature are regional-based, employing techniques that either extract regional features to determine where lesions are present [168], use region growing methods [30], adaptive thresholding [169], or regional difference filters [170]. Many of these segmentation methods require some sort of initialization or decision-making process for parameters, such as the seed points for region growing or the optimal threshold for adaptive thresholding, which are often chosen through optimization algorithms such as the sparse reconstruction algorithm or particle swarm optimization.

Similarly to segmentation techniques for thyroid nodules, many methods here focus on the typical liver cyst appearance in ultrasound images, often overseeing the automatic segmentation of hemangioma or metastasis. Jain and Kumar [170] in their study focused on the automatic segmentation of both typical liver cyst as well as hemangioma, using region-difference filters that evaluate the maximum difference of the average of two regions of the window around the middle pixel. The authors analyzed 56 images and also compared their results with traditional maximum a posteriori-Markov random field, Chan-Vese active contours, and active contour region-scalable fitting energy methods and found the highest accuracy and the fastest implementation when compared to these other methods. The downside of this algorithm is the fact that the parameters necessary for a correct implementation of the method were determined empirically.

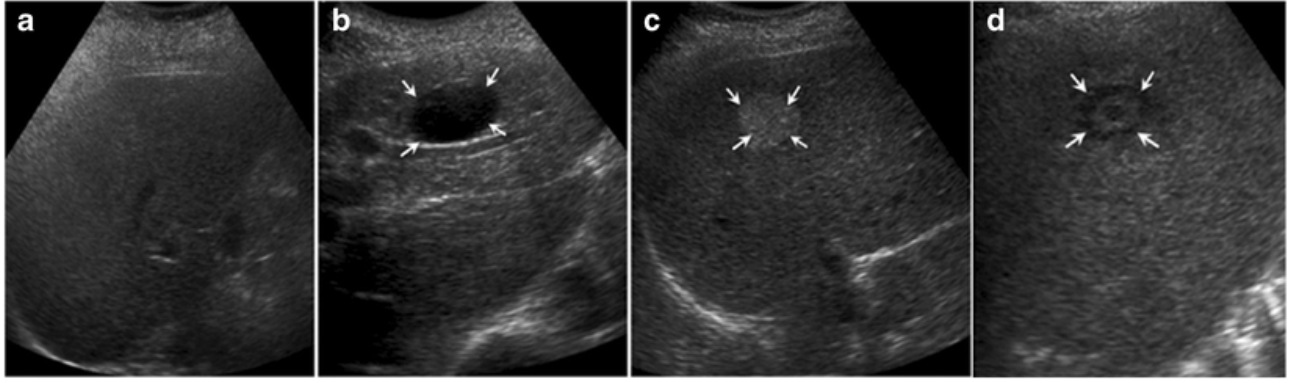


Figure 9. Conventional gray scale B-mode liver US images. (A) Normal liver. (B) Typical cyst. (C) Typical hemangioma. (D) Typical metastasis. Figure taken with permission from [166].

6. Vascular ultrasound imaging

Ultrasound imaging is extensively used in vascular studies and can be divided into three main categories: (1) Plaque and 3D carotid artery imaging, (2) intravascular ultrasound (IVUS) imaging and (3) common carotid artery (CCA) imaging and intima-media thickness (IMT) measurement.

Figure 10 shows some example images and segmentation for each of these three categories.

Artery geometry is well defined and repeatable, having a circular transverse section, a three-layered wall and lumen filled with blood. In ultrasound imaging, blood is anechoic so the lumen of the artery is typically black in the image, whereas the first two layers (going outwards from the lumen) of the artery wall, the intima and media layers, are typically merged together due to image resolution to form the intima-media complex. Based on the projection of the acquired ultrasound image, the artery can appear either as a circular black region with the surrounding walls or as a black “rectangle” surrounded by the proximal and distal wall regions, in transverse and longitudinal projections, respectively.

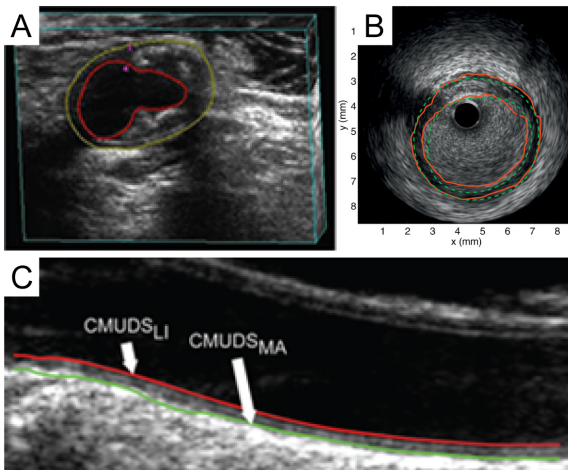


Figure 10. Examples of segmentation in vascular ultrasound imaging. (A) Example transverse view of the CCA with overlaid manual segmentations of the MAB (yellow) and LIB (red) from 3DUS images. Taken and modified with permission from [171]. (B) Example intravascular ultrasound image with segmentation. Red contours: borders detected with algorithm. Dashed curves: manually traced boundaries. Figure taken with permission from [74]. (C) Common carotid artery wall layers segmentation by dual snake algorithm. CMUDS: Carotid Measurement Using Dual Snakes; LI: lumen-intima; MA: media-adventitia. Figure taken with permission from [25].

Plaque and 3D

Carotid plaque segmentation was first proposed on 2D longitudinal images [24], [172]–[174]. Subsequently, using the automatic segmentations, plaque characterization using the pixel intensities has been studied to obtain a sort of “virtual histology” analysis of the plaque [175]–[178], and atherosclerotic risk stratification can be done using, for example, texture-based features [179].

Recently, research in this area has instead focused more on 3D ultrasound imaging of the plaque. In fact, 3D carotid artery ultrasound imaging helps the visualization, measurement (volume) and a more comprehensive characterization of the plaque [180]. Moreover, it also provides the ability to monitor both plaque progression and regression in addition to identifying vulnerable plaques [181]–[183]. With these 3D ultrasound scans, the slices making up the volume typically present the artery in a transverse position. The variability of plaque composition, including calcium-rich plaques which appear hyperechoic in the US image or more lipid-rich plaques which appear hypoechoic, and the very high variability in shape and size of plaques make the automatic segmentation a very challenging task.

In fact, the majority of algorithms found in literature are based on active contours but require some user-interaction to initialize the segmentation by placing anchor points, either by manually segmenting the carotid artery walls or an existing plaque in 3D ultrasound images [158]. Active contour or level set models are the technique of choice in this application due to the fact that they can incorporate various features of the image and can typically adapt well to the different shapes of plaque that may be present.

The active contour models that are used for fine segmentation typically incorporate both image intensity but also other features of the image, such as structural information [184], local region-based image information [171], or a smoothness energy [53] in order to try to reduce leaking at low-contrast boundaries and provide an accurate segmentation.

A technique worthy of being mentioned here is the one presented by Ukwatta et al. [171] in 2013. Their study is the first direct 3D algorithm for segmenting both the media-adventitia boundary (MAB) and the lumen-intima boundary (LIB) presented in literature. Moreover, their algorithm implemented a number of interesting features to provide an accurate segmentation, including integrating both regional and boundary-based image statistics, expert initializations, a smoothness term, and an anatomically motivated boundary separation which constrains the LIB segmentation based on the MAB segmentation which is obtained first. The technique heavily relies on the manual placement of anchor points, but still reduces the complexity of the manual interaction and provides a noticeable time reduction in elaboration, reporting a decrease from average 8.3 minutes for manual segmentation to 1.72 minutes for semi-automatic segmentation.

Intravascular ultrasound imaging (IVUS)

Intravascular ultrasound imaging is the most extensively used imaging modality for coronary plaques because (1) it supports real-time cross-sectional arterial wall grayscale images, (2) the images combined with processing of RF reflected signals are used for the identification of plaques, and (3) these IVUS images can help in making accurate therapeutic decision [185]. Virtual histology of IVUS images has also been extensively researched, but is outside this paper’s scope.

IVUS images present high scattering from red blood cells inside the lumen, making the detection of the luminal border challenging, whereas the hyperechogenic border of the adventitia layer provides an easier interface to segment.

IVUS images suffer from numerous acquisition artifacts which make segmentation more challenging. Specifically, the five main artifacts that are present in these images are: guide wire presence, ring-down, non-uniform rotational distortion, reverberation and discontinuity at 0° in the Cartesian domain [185]. The presence of calcified plaques and motion of both the catheter and heart also add challenges to the segmentation process.

Katouzian et al. [185] provided a comprehensive up to date review on segmentation methods in intravascular ultrasound images in 2012. Here the segmentation techniques were divided into: (1) edge tracking and gradient-based, (2) active contours-based, (3) statistical and probabilistic-based, and (4) multiscale expansion-based. Research over the last few years has shown the development of other techniques that are typically statistical and probabilistic-based, focusing on the use of the fast-marching method (FMM) [75], [186].

Edge-tracking and gradient-based techniques are typically semi-automatic and require a precise initialization. They also typically rely on an energy minimization (optimization) framework in order to achieve an accurate segmentation [187], [188]. Classic active contours typically do not perform well on IVUS images due to the numerous challenges listed previously, so authors employing these methods almost always modify the energy terms or incorporate some kind of pre-processing technique prior to the use of a deformable model [189]. Statistical and probabilistic-based techniques typically assume that grayscale values corresponding to lumen and plaque regions are generated from two different reflector distributions and can be modeled parametrically. This assumption, however, may not be applicable in all situations [190], [191]. Multiscale expansion-based techniques take advantage of spectral analysis or spatial-frequency-localized expansions, showing however some limitations due to the attenuation of signals in regions far from the transducer [192].

Common carotid artery (CCA) and intima-media thickness (IMT) measurement

Common carotid artery ultrasound imaging is extensively used for the calculation of the intima-media thickness (IMT), a widely-used indicator of cerebrovascular and cardiovascular risk [193]. Segmentation algorithms that focus on the IMT measurement almost always focus on the automatic identification of two important artery wall boundaries on the far wall in longitudinal ultrasound images: the lumen-intima (LI) border and the media-adventitia (MA) border.

Longitudinal US images of the carotid artery are typically quite well-defined and repeatable, with the general structure of the hypoechoic lumen and the hyperechoic adventitia far wall. However, different carotid geometry, the possible presence of the jugular vein, and the possible presence of backscattering in the lumen make automatic segmentation not an easy task.

Molinari et al. [7] presented a comprehensive review on IMT measurement and carotid wall segmentation strategies in 2010. Loizou [194] also provided a review of on segmentation methods of carotid artery image and videos in 2014.

The most common techniques used for the coarse localization of the carotid artery within the ultrasound image frame take advantage of the fact that the lumen is echogenic or that the adventitial wall is hyperechoic, often implementing techniques based on local statistics [41], [44].

On the other hand, fine segmentation techniques used to segment the actual lumen-intima (LI) and media-adventitia (MA) borders vary greatly, ranging from methods based on edge tracking or gradient-based [28], optimization and dynamic programming [195]–[197] active contours [22], transform-based [81], [198] and more recently also neural networks [99]. Each of these techniques

present their own pros and cons. Specifically, edge tracking and gradient-based techniques are typically computationally inexpensive and can be easily implemented in real time. However, carotid geometry variability and vessels that are not horizontal in the image present a challenge and these techniques rely greatly also on the operator's ability to select a correct focus position, which drastically changes the image grayscale representation. Dynamic programming and active contour methods are both iterative and therefore are a bit more computationally expensive, but have the upside of being able to also include morphological features of the artery, by giving more weight or setting parameters to control the final "shape" of the border. Because of the necessity of fine-tuning, however, carotid artery images with a variable amount of lumen noise or with a very different geometry can present segmentation errors. Active contours also have the issue of being very dependent on the initialization, which dynamic programming techniques do not present. Transform-based techniques are intrinsically less sensitive to the presence of noise, but rely heavily on the fact that the artery must be present in the image as horizontal and straight. Methods based on machine learning and neural networks present the typical advantages and disadvantages of these types of systems, being able to learn in time and incorporate more complex features of the image, but being heavily dependent on the images used to train the neural network and perhaps not being able to adapt very well to images coming from a different database or with various levels of noise and artery geometry.

Another point to mention is that according to the Mannheim consensus, the carotid IMT should be measured within a region free of plaque with a clearly identified double-line pattern along a 10 mm segment [199]. Most automated techniques calculate one specific value for the IMT found on the entire image. Regarding this point, a method that can be noted is the one developed by Ikeda et al. [200], which detects the carotid bulb edge, a reference marker for measurements of the carotid IMT. The method then automatically calculates segment-based IMT measurements, using 10 mm segments proximal to the bulb edge. The methodology used an integrated approach which combines carotid geometry and pixel-classification paradigms.

Table 4 shows some validation results of IMT segmentation methods found in literature. It should be noted that while almost all IMT algorithms show performance results in terms of IMT error (absolute or not), a direct comparison can still be difficult because of the numerous methods available to calculate the distance between two boundaries. Some metrics include the mean absolute distance which is extensively used but is based on the vertical distance between the two borders, which can present an error when the carotid artery is not horizontal in the ultrasound image. Another metric that has been used extensively is the Polyline distance, which calculates the distance between the points on one border and segments of the other, making it less sensitive to carotid geometry and position in the ultrasound frame.

Table 4. Validation of ultrasound vascular intima-media thickness (IMT) segmentation methods

Reference	Year	Segmentation method	Database size	Performance	
				Measure (distance metric)	Value

Molinari et al. [201]	2010	Feature extraction, line fitting and classification	665	IMT error (Polyline distance metric)	-0.050 ± 0.285 mm
Molinari et al. [16]	2011	Edge flow and heuristics	300	IMT error (Polyline distance metric)	0.043 ± 0.097 mm
Loizou et al. [23]	2015	Active contours	976 (no CVD)	Wilcoxon rank sum (Mean absolute distance)	Left CCA: p=0.72 Right CCA: p=0.67
			125 (CVD)	Wilcoxon rank sum (Mean absolute distance)	Left CCA: p=0.92 Right CCA: p=0.64
Xiao et al. [91]	2015	Markov random field models	80	IMT absolute error (Mean absolute distance)	0.024 ± 0.023 mm
Menchòn-Lara et al. [96]	2016	Machine learning and artificial neural networks	67	IMT error (Mean absolute distance)	0.058 ± 0.034 mm
Zahnd et al. [79]	2017	Dynamic programming in 3D space	60 – training 184 – validation	IMT error (Median radial distance)	0.066 ± 0.090 mm
Ikeda et al. [65]	2017	Carotid geometry and pixel classification	649	IMT error (Polyline distance metric)	0.011 ± 0.003 mm

7. Musculoskeletal

Musculoskeletal ultrasound analysis can be divided into two macro sectors: automatic muscle thickness calculation and fascicle segmentation and tracking. In the ultrasound image, the muscle is typically segmented by identifying the superficial and deep aponeuroses, which are both typically present in the ultrasound image as hyperechoic bands that go across the image width in a traditional longitudinal scanning. Similarly, muscle fascicles in the ultrasound image are present in between two aponeuroses and are displayed as hyperechoic bands which are often interrupted. The muscle fascicles present a certain angle with respect to the deep aponeuroses, which is called the pennation angle. **Figure 5** shows an example of a musculoskeletal ultrasound image.

As far as muscle thickness calculation goes, this measurement has been extensively used in physiological and clinical studies to investigate the adaptations in muscle size occurring with training, disuse atrophy, aging, and pathological conditions [202]–[208].

The presence of speckle and pathology conditions, such as sarcopenia or loss of muscle mass due to ageing, can affect the quality of the images and present a challenge in automatic muscle thickness measurement.

Most works present in literature are focused on the automatic segmentation of a specific muscle, and the techniques are typically based on finding the upper and lower aponeurosis through the Hough transform or other similar line detection algorithms [88], [89] in longitudinal muscle US images. These techniques rely on the fact that the aponeurosis are hyperechoic and run across the entire image width, and segmentation results can be improved by enhancing these hyperechoic regions [88], but could present an issue when considering pathology cases.

An important work found in literature regarding muscle thickness measurement is the one proposed by Caresio et al. [98], a fully automated MUSA algorithm (Muscle UltraSound Algorithm) that considered four different muscles. Their approach first located the aponeuroses candidates through the application of a Sobel gradient, a vertical first-order derivative Gaussian filter. A heuristic process was then applied to select the final aponeuroses locations. The MUSA algorithm was tested on rectus femoris, vastus lateralis, tibialis anterior, and medial gastrocnemius muscle ultrasound images and compared with the manual measurements obtained by three operators.

Table 5 summarizes the validation results of a few muscle thickness segmentation techniques. As can be seen, the intraclass correlation coefficient is often used to validate the performance of the segmentation algorithm in muscle ultrasonography. Using this metric, it can be noted that the method developed by Caresio et al. [98] not only showed the highest ICC among the other algorithms, but was also more versatile, providing very promising results on four muscles whereas all the other techniques focused on measuring the muscle thickness for only one muscle.

Table 5. Validation of ultrasound muscle thickness segmentation methods.

Reference	Year	Segmentation method	Database size (Distance metric)	Performance	
				Measure	Value
Han et al. [88]	2013	Gabor filtering and Revoting Hough Transform	300 (3 subjects, 1 muscle) (Mean Euclidean distance)	Intraclass correlation coefficient	0.975
				Standard Error of measurements	0.27
				Minimal detectable changes	0.75
Han et al. [88]	2013	Multiscale vessel enhancement and Revoting Hough Transform	300 (3 subjects, 1 muscle) (Mean Euclidean distance)	Intraclass correlation coefficient	0.966
				Standard Error of measurements	0.31
				Minimal detectable changes	0.86
Li et al. [89]	2013	Radon transform	6 sequences (250 frames/	Correlation coefficient	0.95 ± 0.01

		and optical flow	sequence, 1 muscle)	Difference	-0.05 ± 0.22 mm
			(Vertical distance between points)		
Caresio et al. [98]	2017	First order derivative filtering and Heuristics	200 (50 subjects, 4 muscles)	Intraclass correlation coefficient (2,1)	0.99 for all 4 muscles
			(Centerline distance)		

As far as fascicle recognition goes in B-mode ultrasound images, research has mainly focused on either fascicle length or fascicle orientation tracking in ultrasound image sequences [209]. The majority of these techniques, however, either (1) require a manual initialization for the successive tracking or the manual placement of a region of interest, or (2) do not present a real segmentation issue but the extraction of the main orientation of objects in the image through radon transforms or wavelet analysis [82], [209]–[214].

A few other musculoskeletal applications include: spinous process and its acoustic shadow segmentation in vertebral ultrasound images [71], knee meniscus segmentation [215], peripheral nerve segmentation [72], [90], [216], and supraspinatus tendon segmentation [217].

8. Obstetrics

Ultrasound imaging has been used since its establishment in the early 1980s for monitoring fetal growth during pregnancy [218]. Fetal age, fetal growth, fetal aneuploidy or down syndrome [219] can be determined or possibly diagnosed based on biometric measurements taken from the ultrasound image, such as the head circumference and nuchal translucency. **Figure 11** shows some example ultrasound images of the fetal head, femur, abdomen and whole fetus.

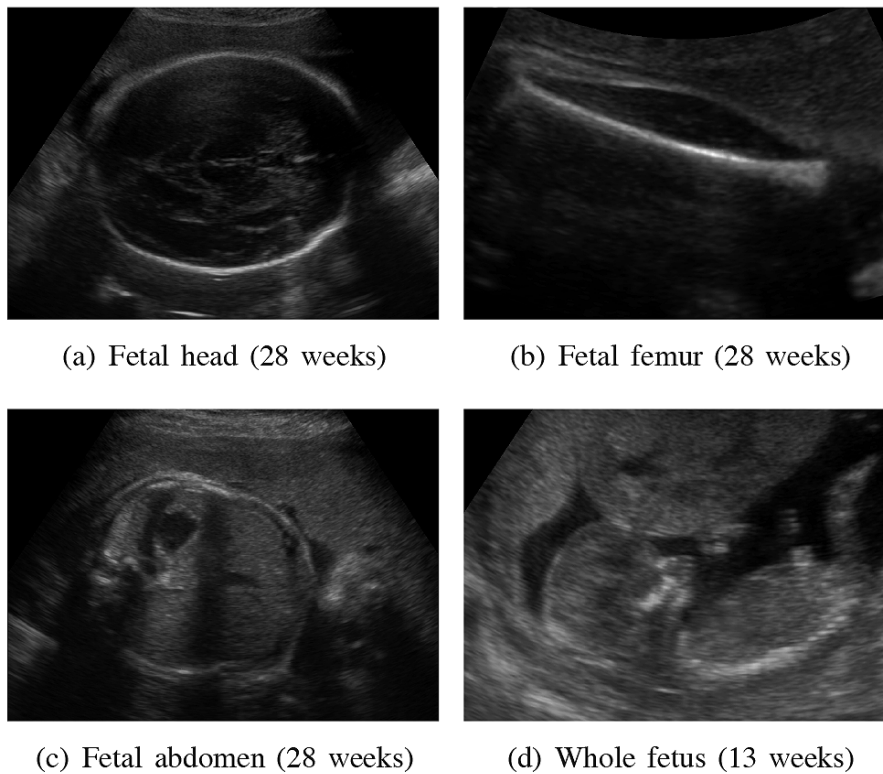


Figure 11. Ultrasound images of the (A) fetal head, (B) fetal femur, (C) fetal abdomen, and (D) the whole fetus. Figure taken with permission from [220].

The majority of research in the automatic localization of fetal structures has focused on the head and femur detection.

In the ultrasound image, the fetal head presents clear boundaries and texture similarities in individuals, making it a common target to automatic segmentation. However, due to ultrasound contrast physics, the left and right borders of the skull are often not clearly portrayed. The fetal femur can tend to lack internal texture but usually presents strong edges in most of the contour except for in the extremities [220].

Segmentation methods for the fetal head and femur detection vary greatly, including the Hough transform, morphologic operators, and active contours, but recent research has focused a lot on the calculation of features and subsequent classification, including Haar-like features [61], texton cues [221], and shape information of pixel groups and local statistics [67]. These methods have the advantage of being able to incorporate many different types of image features and prior knowledge, making the final segmentation more robust.

An interesting work in literature in this research field is the ultrasound grand challenge that was organized during the International Symposium on Biomedical Imaging (ISBI) 2012. The organizers of the challenge then summarized the findings from this challenge in a later publication, evaluating and comparing the segmentation methods presented by the teams that participated in the challenge [220]. For head segmentation, the techniques were based on a signal processing and optimization framework [222], graph-based approaches [223], [224], a boundary fragment model [225], and shape-based recognition and edge detection with multiple thresholds [76]. Two teams presented their works in the femur sub-challenge, based on an adapted shape-based recognition and edge detection with multiple thresholds [76], and a morphology-based approach [226].

A general finding from the grand challenge was that signal processing, machine learning and graph-based methods achieved good results as they used the entire image. Contrarily, intensity and

gradient-based methods showed a lower performance, due to the fact that they focused more on the appearance of the objects of interest, which indicate high variability [220].

A few other applications include nuchal translucency detection [227]–[231], cerebral segmentation on ultrasound volumes [102], [232], [233], the standard plane localization [234], [235], and the segmentation of the fetal aorta [236], [237].

9. *Gynecology*

Gynecologic ultrasonography, in which the female pelvic organs are imaged, is another important application for ultrasound imaging. In fact, it is commonly used to image the uterus, the ovaries, and the Fallopian tubes. Ultrasound image segmentation in gynecologic applications usually focuses on detecting and/or segmenting uterine fibroids [29], [238]–[241] and ovary follicles [73], [242]–[244]. The segmentation of ovarian follicles is important for assessing the physiological status of individual follicles and monitoring their growth in women undergoing assisted reproductive therapy. **Figure 12** shows some example ultrasound images of ovarian follicles and their automatic and manual segmentation [73]. Research on the segmentation of uterine fibroids has recently mostly focused on its necessity for a correct High Intensity Focused Ultrasound (HIFU) therapy.

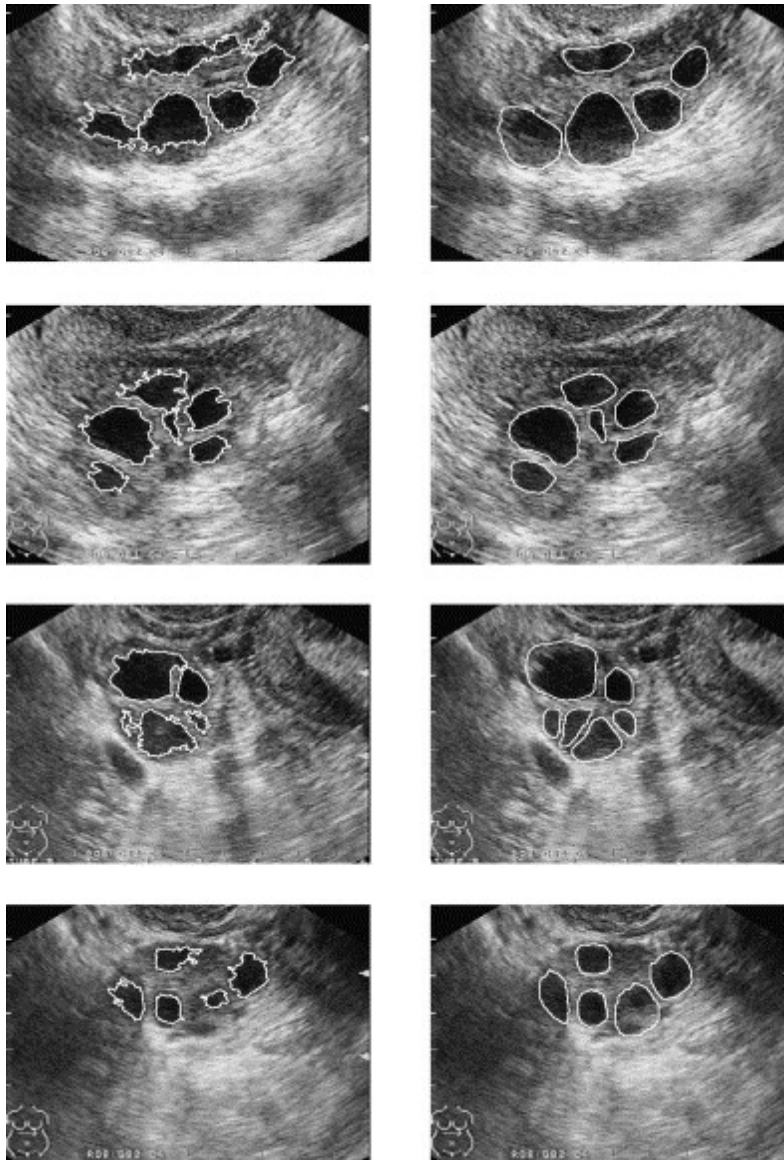


Figure 12. Example ultrasound images of ovarian follicles. Left column: follicles segmented by a computer algorithm. Right column: manual segmentation of follicles. Figure taken with permission from [73].

In ultrasound images, the ovary is typically presented as a medium intensity and homogeneous structure, whereas the ovarian follicles are hypoechoic structures within the ovary. Clinically, it is important to count the number of follicles and calculate their diameter; if there are more than 12 follicles present, a Poly Cystic Ovarian Syndrome (PCOS) is diagnosed. Small follicles can often overlap within the ultrasound image, making a manual counting prone to error and complicating the automatic segmentation process. Moreover, the presence of artifacts, especially if hyperechoic structures are present towards the top of the image, and the variability of follicle shape present other challenges to overcome during an automatic segmentation procedure. Another clinical interest is the analysis of follicle walls during reproductive therapy, since those that are destined to ovulate are thinner and have a higher ultrasonographic signal intensity and a smoother and more even texture.

In this application, thresholding is very commonly used. Due to the complexity of the analyzed images, the best threshold is often found through an optimization technique, such as an entropy

method [243], or a particle swarm optimization [242]. Region growing has also been used as a solution for this segmentation problem [73]. These types of methods often perform reasonably well but also require a segmentation refinement, since thresholding the image will often include some noise. Nevertheless, these issues can typically be mitigated through morphological operations or by extracting some features from the segmented objects, such as the area, shape, etc. The majority of methods found in literature focus on only the follicle inner border segmentation.

To note here is the method presented almost 20 years ago by Krivanek and Sonka [62], which semi-automatically segmented both the inner and the outer border of the follicles. The method was based on the watershed transform and thresholding and required the user to identify the follicle of interest. While presenting interesting results and a technique that could now be rendered completely automatic, not many advances in this field focusing on inner and outer follicle boundaries were found in literature.

When considering the uterine fibroid application, research has focused much on accurate fibroid segmentation in order to correctly guide HIFU treatment. Fibroids appear in the ultrasound image as a hypoechoic region, and the main challenge here is dealing with the fact that a HIFU guidance device produces images that have a much lower quality and signal-to-noise ratio when compared to traditional ultrasound images.

In this application, segmentation methods often incorporate active contours or shape priors in some way [29], [239], [240], but many of these techniques still require manually inserting the target area or are based on US image sequences.

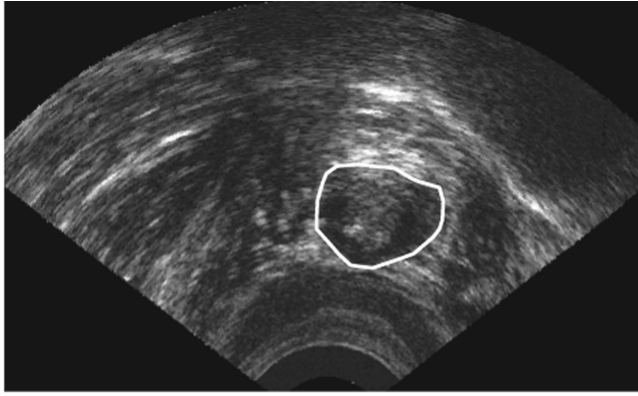
A recent work that is completely automatic was presented by Zhang et al. [245] in 2016. Their method took a different approach compared to those found in literature and was based on dividing the image into superpixels and extracting features from homogeneous regions. Their method showed good results on 50 images, but was not real time, requiring approximately 13 seconds to process one image.

10. Prostate

Three-dimensional trans-rectal ultrasound (TRUS) imaging is a necessary tool to diagnose prostate cancer, as prostate boundaries assist in cancer diagnosis and treatment. Specifically, real-time target anatomy segmentation is crucial in brachytherapy, which consists in the permanent implantation of small radioactive seeds and adjacent tissue, and in TRUS-guided biopsies.

The main challenges in this segmentation problem are due to the fact that prostate shape and size varies greatly, due to bladder and rectum fillings, the patient conditions, prostate deformation, the development of edema during the procedure, and also cancer evolution rate and characteristics [246].

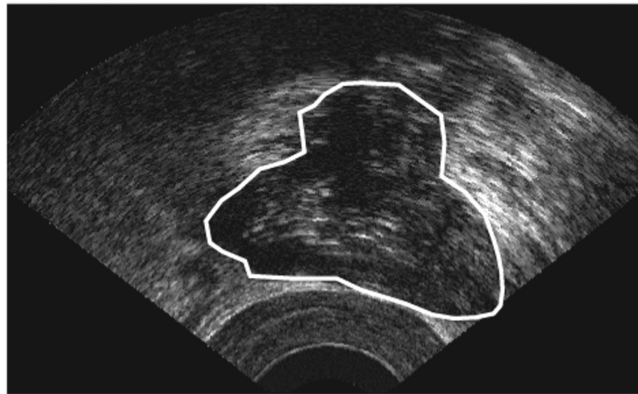
Figure 12 shows an example ultrasound image of the prostate obtained at apex, mid-gland, and base regions.■



(a)



(b)



(c)

Figure 13. Example prostate ultrasound images obtained at (A) apex, (B) mid-gland and (C) base regions. Figure taken with permission from [54].

In prostate ultrasound imaging, there is a vast selection of segmentation strategies, ranging from simple edge-guided to shape prior and classification techniques. Noble and Boukerroui [3] presented a comprehensive overview of prostate ultrasound imaging techniques until 2006, but many of them are semi-automatic [217]–[219], and more recently Ghose et. al [6], [250] also presented a survey on segmentation methodologies using various imaging modalities, including ultrasound.

More recent developments have seen more of a focus on supervised learning frameworks, based on shape and probability priors or level sets [54], [63], [64] and less focus on edge-guided or pixel region-based techniques. The implementation of these more advanced segmentation techniques make the method typically more robust to shape, contrast, and size of the object within the image. The segmentation algorithms based on shape priors obviously require the construction of prior models which constrain image segmentation and also require more computational cost. Many prostate segmentation techniques also tend to evaluate segmentation results in the mid-gland area, where the prostate boundaries are clearer.

An interesting work in this application was presented by Yu et al. [54] in 2016. Their technique was completely automatic, in which the initial first contour of the volume was found using a radial bas-relief technique [251]. Subsequently, the initial contour was deformed using the detailed and approximate coefficients generated using dyadic wavelet transforms, and the segmented border on the first frame was then propagated to the next frame as the initial boundary until all frames were segmented. This study also presented an important comprehensive comparison with other published TRUS segmentation methodologies that is also presented here in Table 6 along with the comparison with the other segmentation techniques.

As can be seen from Table 6, the mean absolute difference (MAD) is often used as a way to evaluate the performance of TRUS segmentation techniques, along with the use of the Dice similarity coefficient, which is also extensively used in other applications. The semi-automated techniques show some of the best performing results, which is to be expected as user-interaction can mitigate many segmentation challenges. Still, the completely automatic technique by Ghose et al. [252] that is based on posterior probability and multiple mean parametric models showed very promising results with a $MAD = 0.49 \pm 0.20$ mm; however, the database that was used was quite small, consisting of only 46 images. Of the completely automatic techniques with a decent sized database, it is to note that the technique by Yu et al. [54] showed an important increase in performance results (i.e., decrease in MAD) from the other previous techniques.

Table 6. Validation of TRUS segmentation methods

Reference	Year	Segmentation method	Database size	Performance	
				Measure	Value
Knoll et al. [248]	1999	Automatic dyadic wavelet transforms and active contours with shape priors	77 images (11 patients)	Mean absolute difference	2.61 mm
Ladak et al. [253]	2000	Semi-automatic discrete dynamic contour	117 images (19 patients)	Mean absolute difference	0.55 \pm 0.40 mm
Shen et al. [254]	2003	Automatic Gabor filter bank and statistical shape model	8 images (8 patients)	Mean absolute difference	1.28 \pm 0.35 mm

Chiu et al. [255]	2004	Semi-automatic dyadic wavelet transform and discrete dynamic contour	114 images (6 patients)	Mean absolute difference	0.58 ± 0.18 mm
Cosìo et al. [256]	2008	Automatic pixel classification and active shape model	22 images (4 patients)	Mean absolute difference	1.74 ± 0.69 mm
Yan et al. [257]	2011	Automatic global population-based and patient-specific local shape statistics and deformable model	301 images (19 patients)	Mean absolute difference	1.65 ± 0.47 mm
Ghose et al. [252]	2011	Automatic posterior probability and multiple mean parametric models	46 images (23 patients)	Mean absolute difference	0.49 ± 0.20 mm
Ghose et al. [63]	2013	Automatic statistical shape and probability priors	126 images (23 patients)	Dice similarity coefficient Mean absolute difference	$91 \pm 1\%$ 1.26 ± 0.60 mm
Wu et al. [258]	2013	Automatic Gabor filter banks and non-parametric kernel density estimation shape prior	132 images (132 patients)	Mean absolute difference	1.21 ± 0.85 mm
Qiu et al. [64]	2014	Semi-automatic coherent continuous max-flow model (CCMFM) enforcing prostate axial symmetry	8750 images (25 patients)	Dice similarity coefficient	$93.2 \pm 2.0\%$
Wu et al. [259]	2015	Automatic level set integrating shape priors, intensity transition, texture features	132 images (132 patients)	Mean absolute difference	1.06 ± 0.53 mm
Yu et al. [54] [95]	2016	Automatic radial basis relief and dyadic wavelet transforms	336 images (15 patients)	Mean absolute difference	0.79 ± 0.26 mm

6. Discussion

This paper aims to provide a comprehensive review of the literature on automatic techniques that are used in B-mode ultrasound imaging. Different from other reviews which typically focus on specific applications, this review focuses instead on the various segmentation techniques that are available, providing the reader with an overview of the methods currently available. A total of 11 segmentation techniques were presented and expounded upon, focusing also on whether the examined method can be used for a fine segmentation of the object of interest or if it is typically only used for a coarse localization of a tissue/organ

within the ultrasound frame in two-step segmentation methods (i.e., such as the localization of the carotid artery in the US frame and the final segmentation of the artery boundaries for IMT calculation).

The methods that are presented in this review are: active contours, shape priors, superpixel and classification, texture and classification, local statistics/pixel intensity, edge-tracking, optimization techniques, transform-based, data-mining, heuristics, and machine learning.

Active contours can be considered a type of optimization technique because they aim to search for the balance between the internal and external energy forces, but were expounded upon separately due to the large use of these kinds of specific segmentation techniques. Moreover, active contours optimize an initial contour that must be defined (automatically or manually), whereas the majority of other optimization segmentation techniques do not require an initial contour. Optimization techniques can more easily adapt to variations in shape of the object of interest but heavily rely on a proper parameter or function selection. This makes it more challenging to accurately segment both images with high and low contrast or with high and low signal-to-noise ratios (SNR). Moreover, these techniques are typically employed and optimized on a certain database and must often be altered before using on a different database. However, a great advantage of these techniques is that they can often consider edge and shape together.

Shape priors are very robust to noises and artifacts. The presence of image-degrading characteristics does not have a big influence on the final segmentation, as a certain general shape is searched for and found within the image frame. However, this technique is quite computationally expensive and needs a training set which will determine the shape to be located. Transform-based techniques (i.e., Hough transform) also search within the image frame for a certain shape, but do not require a training set. Due to the fact that both of these methods search for an already determined shape, a variation of the expected shape, which often happens in the case of pathology, could risk not being correctly located.

Local statistics/pixel intensity and edge-tracking segmentation methods rely basically only on the intensity and intensity distribution within the image. Since edges and therefore intensity depend on transducer position, these techniques perform well when the object of interest is present in the image with a direction that is perpendicular to the ultrasound signal propagation, with relatively low noise and artifacts. These techniques typically present a low computational cost and can therefore be extremely useful with real-time applications.

Many of the techniques present the need to classify specific features or regions within the ultrasound frame. Specifically, superpixel and classification, texture and classification, data-mining, heuristics and machine learning techniques all require some sort of higher knowledge in order to correctly classify pixels (heuristics) or regions (superpixel and classification, texture and classification, data-mining, machine learning). Texture is a specific feature of the image, but was not included in data-mining techniques because it does not necessarily rely on the application of a feature reduction or selection algorithm, which characterizes data-mining techniques. At the same time, however, texture features are almost always included as some of the initial image features in data-mining methods. The same comments can also be applied to superpixel methods, where specific features are extracted in order to classify each superpixel. Heuristic methods rely on the higher knowledge of the author of the heuristic in order to classify a specific pixel as being of potential interest or not of interest. The heuristic search is done in the exact same way along the entire width of the image or ROI (or considering a subset of the width, i.e., one column every ten columns), making this method sensitive to noise and artifacts, but also very useful and applicable when the object of interest portrays similar characteristics along the image/ROI. Machine learning methods have

acquired much interest recently along with the peak focus on big data. In fact, these techniques focus on the training of the computer with a massive amount of data in order to then correctly classify a pixel/region. A number of different patterns can be captured with the numerous layers in deep learning, and once properly trained, the learned developed system does not need any handcrafted features, unlike many other methods.

After presenting the mainstream segmentation techniques present in literature, focus was then pointed towards specific applications. Ultrasound imaging is continuously growing in clinical applications, due to its real-time imaging, non-ionizing radiation, and inexpensive implementation. This is made evident by the large number of selected applications that were analyzed in this review including abdomen/kidney, breast, cardiology, thyroid, liver, vascular, musculoskeletal, obstetrics, gynecology, and prostate. Since these applications are used for screening for a disease or tracking a specific lesion, it is evident how important it is to be able to both correctly locate the area of interest if applicable, and to standardize the measurement of the quantitative information with automatic algorithms.

A field of research that is also developing is the segmentation of ultrasound images based on the raw radiofrequency (RF) signal and not solely on beamformed envelope B-mode images. The process of B-mode image formation unfortunately loses some information such as signal phase; phase information has been suggested to be another way to extract details from an image and is also invariant to both intensity and magnitude [3]. For some examples of techniques based on the ultrasound RF signals, please refer to [260]–[265]. Image segmentation using the RF signal will most likely continue to evolve in the future, integrating both amplitude and phase information in conjunction with non-RF segmentation techniques to create advanced segmentation methods with more precise segmentation results [266], [267].

B-mode ultrasound imaging will likely only continue to grow, and with that a clear understanding of the segmentation techniques available will aid in the development of enabling technologies within this field. As the previous paragraph also suggested, a future perspective of B-mode image segmentation is the incorporation of more data deriving from the RF signal with other B-mode segmentation techniques. With the development of higher frequency US transducers that can be used in a clinical situation, specific applications that do not require deep imaging within the body will most likely also see a shift in segmentation algorithms, since the higher frequency will give forth images with a much higher resolution, providing greater detail and information that was impossible to distinguish with images acquired with a lower frequency transducer. Finally, with the increase of data available and with researchers hopefully adopting more and more an “open data” mentality, segmentation techniques that are completely automatic and ones that rely on large databases, such as machine learning, will continue to develop and will most definitely be a part of the future of B-mode ultrasound image segmentation.

7. Conclusions

In this paper we reviewed completely automatic localization and segmentation techniques for B-mode ultrasound images, providing insight on both coarse localization and fine segmentation techniques, and analyzing the various methods’ robustness to noise and artifacts. We discussed several clinical applications and segmentation techniques that are used in each application, and finally we looked into the future of ultrasound segmentation techniques.

References

- [1] T. Szabó, *Diagnostic ultrasound imaging : inside out*. Elsevier Academic, 2004.

- [2] V. Shrimali, R. S. Anand, and V. Kumar, "Current trends in segmentation of medical ultrasound B-mode images : a review," *IETE Tech. Rev.*, vol. 26, no. 1, pp. 8–17, 2009.
- [3] J. A. Noble, S. Member, and D. Boukerroui, "Ultrasound image segmentation : a survey," *IEEE Trans. Med. Imaging*, vol. 25, no. 8, pp. 987–1010, 2006.
- [4] H. D. Cheng, J. Shan, W. Ju, Y. Guo, and L. Zhang, "Automated breast cancer detection and classification using ultrasound images : A survey," *Pattern Recognit.*, vol. 43, no. 1, pp. 299–317, 2010.
- [5] S. Khachira, F. Kallel, O. Tankyevych, and A. Ben Hamida, "Speckle reduction and segmentation in echocardiographic images: A comparative study," *Int. Image Process. Appl. Syst. Conf. IPAS 2014*, pp. 1–6, 2014.
- [6] S. Ghose, A. Oliver, R. Martí, X. Lladó, J. C. Vilanova, J. Freixenet, J. Mitra, D. Sidibé, and F. Meriaudeau, "A survey of prostate segmentation methodologies in ultrasound, magnetic resonance and computed tomography images," *Comput. Methods Programs Biomed.*, vol. 108, no. 1, pp. 262–287, 2012.
- [7] F. Molinari, G. Zeng, and J. Suri, "A state of the art review on intima–media thickness (IMT) measurement and wall segmentation techniques for carotid ultrasound," *Comput. methods programs Biomed.*, vol. 100, no. 3, pp. 201–221, 2010.
- [8] M. K. Feldman, S. Katyal, and M. S. Blackwood, "US artifacts.," *Radiographics*, vol. 29, no. 4, pp. 1179–89, 2009.
- [9] R. Wagner, S. Smith, and J. Sandrik, "Statistics of speckle in ultrasound B-scans," *IEEE Trans. sonics Ultrason.*, vol. 30, no. 3, pp. 156–163, 1983.
- [10] A. H. Curiale, G. Vegas-Sánchez-Ferrero, and S. Aja-Fernández, "Influence of ultrasound speckle tracking strategies for motion and strain estimation," *Med. Image Anal.*, vol. 32, pp. 184–200, 2016.
- [11] M. O'Donnell, A. R. Skovoroda, B. M. Shapo, and S. Y. Emelianov, "Internal displacement and strain imaging using ultrasonic speckle tracking," *IEEE Trans. Ultrason. Ferroelectr. Freq. Control*, vol. 41, no. 3, pp. 314–325, May 1994.
- [12] C. P. Loizou, C. S. Pattichis, C. I. Christodoulou, R. S. H. Istepanian, M. Pantziaris, and A. Nicolaides, "Comparative evaluation of despeckle filtering in ultrasound imaging of the carotid artery," *IEEE Trans. Ultrason. Ferroelectr. Freq. Control*, vol. 52, no. 10, pp. 1653–1669, 2005.
- [13] B. K. Singh, K. Verma, and A. S. Thoke, "Objective and optical evaluation of despeckle filters in breast ultrasound images," *IETE Tech. Rev.*, vol. 4602, no. July 2015, pp. 1–15, 2015.
- [14] S. T. Acton, "Deconvolutional speckle reducing anisotropic diffusion," in *International Conference on Image Processing, ICIP*, 2005, vol. 1, no. 11, pp. 5–8.
- [15] Y. Yu and S. T. Acton, "Edge detection in ultrasound imagery using the instantaneous coefficient of variation," *IEEE Trans. Image Process.*, vol. 13, no. 12, pp. 1640–1655, 2004.
- [16] F. Molinari, K. M. Meiburger, G. Zeng, A. Nicolaides, and J. S. Suri, "CAUDLES-EF: Carotid automated ultrasound double line extraction system using edge flow," *J. Digit. Imaging*, vol. 24, no. 6, pp. 1059–1077, 2011.
- [17] A. Ciurte, X. Bresson, O. Cuisenaire, N. Houhou, S. Nedevschi, J. P. Thiran, and M. B. Cuadra, "Semi-supervised segmentation of ultrasound images based on patch representation and continuous min cut," *PLoS One*, vol. 9, no. 7, 2014.

- [18] K. Diaz and B. Castaneda, "Semi-automated segmentation of the prostate gland boundary in ultrasound images using a machine learning approach," in *SPIE Med. Imag*, 2008, vol. 6914, no. 3, pp. 1–8.
- [19] J. Sundholm, T. Gustavsson, and T. Sarkola, "Semi-automatic border detection software for the quantification of arterial lumen, intima-media and adventitia layer thickness with very-high resolution ultrasound," *Atherosclerosis*, vol. 234, no. 2, pp. 283–287, 2014.
- [20] E. Supriyanto, N. M. Arif, A. H. Rusli, and N. Humaimi, "Semi-automatic thyroid area measurement based on ultrasound image," in *15th WSEAS International Conference on Computers*, 2011, no. July, pp. 1–6.
- [21] D. J. Williams and M. Shah, "A fast algorithm for active contours and curvature estimation," *CVGIP Image Underst.*, vol. 55, no. 1, pp. 14–26, Jan. 1992.
- [22] C. P. Loizou, C. S. Pattichis, M. Pantziaris, T. Tyllis, and A. Nicolaides, "Snakes based segmentation of the common carotid artery intima media," *Med. Biol. Eng. Comput.*, vol. 45, no. 1, pp. 35–49, 2007.
- [23] C. P. Loizou, A. Nicolaides, E. Kyriacou, N. Georghiou, M. Griffin, and C. S. Pattichis, "A comparison of ultrasound intima-media thickness measurements of the left and right common carotid artery," *IEEE J. Transl. Eng. Heal. Med.*, vol. 3, pp. 1–10, 2015.
- [24] C. P. Loizou, C. S. Pattichis, S. Member, M. Pantziaris, and A. Nicolaides, "An integrated system for the segmentation of atherosclerotic carotid plaque," *IEEE Trans. Inf. Technol. Biomed.*, vol. 11, no. 6, pp. 661–667, 2007.
- [25] F. Molinari, K. M. Meiburger, L. Saba, G. Zeng, U. R. Acharya, M. Ledda, A. Nicolaides, and J. S. Suri, "Fully automated dual-snake formulation for carotid intima-media thickness measurement: a new approach," *J. Ultrasound Med.*, vol. 31, no. 7, pp. 1123–1136, Jul. 2012.
- [26] F. Molinari, K. M. Meiburger, L. Saba, U. Rajendra Acharya, M. Ledda, A. Nicolaides, and J. S. Suri, "Constrained snake vs. conventional snake for carotid ultrasound automated IMT measurements on multi-center data sets," *Ultrasonics*, vol. 52, no. 7, pp. 949–961, 2012.
- [27] M. Demi and M. Paterni, "The first order absolute moment in low-level image processing," in *Digital Signal Processing*, 1997, pp. 511–514.
- [28] F. Faita, V. Gemignani, E. Bianchini, C. Giannarelli, and M. Demi, "Real-time measurement system for the evaluation of the intima media thickness with a new edge detector," in *2006 International Conference of the IEEE Engineering in Medicine and Biology Society*, 2006, pp. 715–718.
- [29] B. Ni, F. He, Y. Pan, and Z. Yuan, "Using shapes correlation for active contour segmentation of uterine fibroid ultrasound images in computer-aided therapy," *Appl. Math. J. Chinese Univ.*, vol. 31, no. 1, pp. 37–52, 2016.
- [30] W. Wang, J. Li, Y. Jiang, Y. Xing, and X. Xu, "An automatic energy-based region growing method for ultrasound image segmentation," in *International Conference on Image Processing, ICIP*, 2015, vol. 2015, pp. 1553–1557.
- [31] R. Achanta, A. Shaji, K. Smith, and A. Lucchi, "SLIC superpixels compared to state-of-the-art superpixel methods," *IEEE Trans. Pattern Anal. Mach. Intell.*, vol. 34, no. 11, pp. 2274–2282, 2012.
- [32] F. Valckx and J. Thijssen, "Characterization of echographic image texture by cooccurrence matrix parameters," *Ultrasound Med. Biol.*, vol. 23, no. 4, pp. 559–571, 1997.
- [33] T. Tegos, D. Mavrophoros, and M. Sabetai, "Types of neurovascular symptoms and carotid plaque

ultrasonic textural characteristics,” *J. ultrasound Med.*, vol. 20, no. 2, pp. 113–121, 2001.

- [34] R. Acharya, O. Faust, A. Alvin, and S. Sree, “Symptomatic vs. asymptomatic plaque classification in carotid ultrasound,” *J. Med. Syst.*, vol. 36, no. 3, pp. 1861–1871, 2012.
- [35] F. Molinari, C. Caresio, and U. Acharya, “Advances in quantitative muscle ultrasonography using texture analysis of ultrasound images,” *Ultrasound Med. Biol.*, vol. 41, no. 9, pp. 2520–2532, 2015.
- [36] U. R. Acharya, M. R. K. Mookiah, S. Vinitha Sree, D. Afonso, J. Sanches, S. Shafique, A. Nicolaides, L. M. Pedro, J. Fernandes e Fernandes, and J. S. Suri, “Atherosclerotic plaque tissue characterization in 2D ultrasound longitudinal carotid scans for automated classification: a paradigm for stroke risk assessment,” *Med. Biol. Eng. Comput.*, vol. 51, no. 5, pp. 513–523, May 2013.
- [37] U. R. Acharya, O. Faust, S. V. Sree, F. Molinari, R. Garberoglio, and J. S. Suri, “Cost-effective and non-invasive automated benign & malignant thyroid lesion classification in 3D contrast-enhanced ultrasound using combination of wavelets and textures: a class of ThyroScan™ algorithms,” *Technol. Cancer Res. Treat.*, vol. 10, no. 4, pp. 371–380, 2011.
- [38] U. Rajendra Acharya, S. Vinitha Sree, M. Muthu Rama Krishnan, F. Molinari, R. Garberoglio, and J. S. Suri, “Non-invasive automated 3D thyroid lesion classification in ultrasound: A class of ThyroScan™ systems,” *Ultrasonics*, vol. 52, no. 4, pp. 508–520, 2012.
- [39] B. Liu, H. D. Cheng, J. Huang, J. Tian, X. Tang, and J. Liu, “Fully automatic and segmentation-robust classification of breast tumors based on local texture analysis of ultrasound images,” *Pattern Recognit.*, vol. 43, no. 1, pp. 280–298, 2010.
- [40] D. Boukerroui, A. Baskurt, J. Noble, and O. Basset, “Segmentation of ultrasound images—multiresolution 2D and 3D algorithm based on global and local statistics,” *Pattern Recognit. Lett.*, vol. 24, no. 4, pp. 779–790, 2003.
- [41] F. Molinari, K. M. Meiburger, G. Zeng, U. R. Acharya, W. Liboni, A. Nicolaides, and J. S. Suri, “Carotid artery recognition system: A comparison of three automated paradigms for ultrasound images,” *Med. Phys.*, vol. 39, no. 1, p. 378, 2012.
- [42] F. Molinari, G. Zeng, and J. S. Suri, “Intima-media thickness: Setting a standard for a completely automated method of ultrasound measurement,” *IEEE Trans. Ultrason. Ferroelectr. Freq. Control*, vol. 57, no. 5, pp. 1112–1124, 2010.
- [43] F. Molinari, W. Liboni, P. Giustetto, S. Badalamenti, and J. S. Suri, “Automatic computer-based tracings (ACT) in longitudinal 2-D ultrasound images using different scanners,” *J. Mech. Med. Biol.*, vol. 9, no. 4, pp. 481–505, 2009.
- [44] E. G. Sifakis and S. Golemati, “Robust carotid artery recognition in longitudinal B-mode ultrasound images,” *IEEE Trans. Image Process.*, vol. 23, no. 9, pp. 3762–3772, Sep. 2014.
- [45] F. Molinari, C. S. Pattichis, G. Zeng, L. Saba, U. R. Acharya, R. Sanfilippo, A. Nicolaides, and J. S. Suri, “Completely automated multiresolution edge snapper-A new technique for an accurate carotid ultrasound IMT measurement: Clinical validation and benchmarking on a multi-institutional database,” *IEEE Trans. Image Process.*, vol. 21, no. 3, pp. 1211–1222, 2012.
- [46] C. H. Wu and Y. N. Sun, “Segmentation of kidney from ultrasound B-mode images with texture-based classification,” *Comput. Methods Programs Biomed.*, vol. 84, no. 2–3, pp. 114–123, 2006.
- [47] Q. H. Huang, S. Y. Lee, L. Z. Liu, M. H. Lu, L. W. Jin, and A. H. Li, “A robust graph-based segmentation method for breast tumors in ultrasound images,” *Ultrasonics*, vol. 52, no. 2, pp. 266–275, 2012.

- [48] W. Wang, L. Zhu, J. Qin, Y.-P. Chui, B. N. Li, and P.-A. Heng, "Multiscale geodesic active contours for ultrasound image segmentation using speckle reducing anisotropic diffusion," *Opt. Laser. Eng.*, vol. 54, no. 0, pp. 105–116, 2014.
- [49] D. Barbosa, T. Dietenbeck, J. Schaerer, J. D'hooge, D. Friboulet, and O. Bernard, "B-Spline explicit active surfaces: an efficient framework for real-time 3-D region-based segmentation," *IEEE Trans. Image Process.*, vol. 21, no. 1, pp. 241–251, Jan. 2012.
- [50] J. Bersvendsen, F. Orderud, R. Massey, K. Fossa, O. Gerard, S. Urheim, and E. Samset, "Automated segmentation of the right ventricle in 3D echocardiography: a Kalman filter state estimation approach," *IEEE Trans. Med. Imaging*, vol. 62, no. c, pp. 1–1, 2015.
- [51] I. Legakis, M. A. Savelonas, D. Maroulis, and D. K. Iakovidis, "Computer-based nodule malignancy risk assessment in thyroid ultrasound images," *Int. J. Comput. Appl.*, vol. 33, no. 1, 2011.
- [52] E. Ukwatta, J. Awad, a D. Ward, D. Buchanan, J. Samarabandu, G. Parraga, and a Fenster, "Three-dimensional ultrasound of carotid atherosclerosis: semiautomated segmentation using a level set-based method.," *Med. Phys.*, vol. 38, no. 5, pp. 2479–2493, 2011.
- [53] H. M.M., A. K., Z. L., L. B.K., and S. S., "Semiautomatic segmentation of atherosclerotic carotid artery wall volume using 3D ultrasound imaging," *Med. Phys.*, vol. 42, no. 4, 2015.
- [54] Y. Yu, Y. Chen, and B. Chiu, "Fully automatic prostate segmentation from transrectal ultrasound images based on radial bas-relief initialization and slice-based propagation," *Comput Biol Med*, vol. 74, pp. 74–90, 2016.
- [55] M. Noll, X. Li, and S. Wesarg, "Automated Kidney Detection and Segmentation in 3D Ultrasound," Springer, Cham, 2014, pp. 83–90.
- [56] M. Marsousi, K. N. Plataniotis, and S. Stergiopoulos, "Shape-based kidney detection and segmentation in three-dimensional abdominal ultrasound images," in *2014 36th Annual International Conference of the IEEE Engineering in Medicine and Biology Society*, 2014, pp. 2890–2894.
- [57] D. Selvathi and S. Bama, "Phase based distance regularized level set for the segmentation of ultrasound kidney images," *Pattern Recognit. Lett.*, vol. 86, pp. 9–17, Jan. 2017.
- [58] M. Marsousi, K. N. Plataniotis, and S. Stergiopoulos, "An Automated Approach for Kidney Segmentation in Three-Dimensional Ultrasound Images," *IEEE J. Biomed. Heal. Informatics*, vol. 21, no. 4, pp. 1079–1094, Jul. 2017.
- [59] J. Xie, Y. Jiang, and H. Tsui, "Segmentation of kidney from ultrasound images based on texture and shape priors," *IEEE Trans. Med. Imaging*, vol. 24, no. 1, pp. 45–57, 2005.
- [60] M. Hansson, S. S. Brandt, J. Lindström, P. Gudmundsson, A. Jujić, A. Malmgren, and Y. Cheng, "Segmentation of B-mode cardiac ultrasound data by Bayesian Probability Maps," *Med. Image Anal.*, vol. 18, no. 7, pp. 1184–1199, 2014.
- [61] D. Ni, Y. Yang, S. Li, J. Qin, S. Ouyang, T. Wang, and P. A. Heng, "Learning based automatic head detection and measurement from fetal ultrasound images via prior knowledge and imaging parameters," in *International Symposium on Biomedical Imaging*, 2013, pp. 772–775.
- [62] A. Krivanek and M. Sonka, "Ovarian ultrasound image analysis: follicle segmentation," *IEEE Trans. Med. Imaging*, vol. 17, no. 6, pp. 935–944, 1998.
- [63] S. Ghose, A. Oliver, J. Mitra, R. Martí, X. Lladó, J. Freixenet, D. Sidibé, J. C. Vilanova, J. Comet, and F.

- Meriaudeau, "A supervised learning framework of statistical shape and probability priors for automatic prostate segmentation in ultrasound images," *Med. Image Anal.*, vol. 17, no. 6, pp. 587–600, 2013.
- [64] W. Qiu, J. Yuan, E. Ukwatta, Y. Sun, M. Rajchl, and A. Fenster, "Prostate segmentation: An efficient convex optimization approach with axial symmetry using 3-D tRUS and MR images," *IEEE Trans. Med. Imaging*, vol. 33, no. 4, pp. 947–960, 2014.
- [65] N. Ikeda, N. Dey, A. Sharma, A. Gupta, S. Bose, S. Acharjee, S. Shafique, E. Cuadrado-Godia, T. Araki, L. Saba, J. R. Laird, A. Nicolaides, and J. S. Suri, "Automated segmental-IMT measurement in thin/thick plaque with bulb presence in carotid ultrasound from multiple scanners: Stroke risk assessment," *Comput. Methods Programs Biomed.*, vol. 141, pp. 73–81, 2017.
- [66] C. Y. Chang, Y. F. Lei, C. H. Tseng, and S. R. Shih, "Thyroid segmentation and volume estimation in ultrasound images," *IEEE Trans. Biomed. Eng.*, vol. 57, no. 6, pp. 1348–1357, 2010.
- [67] A. I. L. Namburete and J. A. Noble, "Fetal cranial segmentation in 2D ultrasound images using shape properties of pixel clusters," in *2013 IEEE 10th International Symposium on Biomedical Imaging*, 2013, pp. 720–723.
- [68] W. Mahani Hafizah and E. Supriyanto, "Comparative evaluation of ultrasound kidney image enhancement techniques," *Int. J. Comput. Appl.*, vol. 21, no. 7, pp. 15–19, 2011.
- [69] P. Jiang, J. Peng, and G. Zhang, "Learning-based automatic breast tumor detection and segmentation in ultrasound images," in *2012 9th IEEE International Symposium on Biomedical Imaging (ISBI)*, 2012, pp. 1587–1590.
- [70] C. Ye, V. Vaidya, and F. Zhao, "Improved mass detection in 3D automated breast ultrasound using region based features and multi-view information," *Eng. Med. Biol. Soc. 2014 36th Annu. Int. Conf. IEEE*, pp. 2865–2868, 2014.
- [71] F. Berton, F. Cheriet, M.-C. Miron, and C. Laporte, "Segmentation of the spinous process and its acoustic shadow in vertebral ultrasound images," *Comput. Biol. Med.*, vol. 72, pp. 201–211, 2016.
- [72] J. J. Giraldo, M. A. Alvarez, and A. A. Orozco, "Peripheral nerve segmentation using nonparametric Bayesian hierarchical clustering," in *2015 37th Annual International Conference of the IEEE Engineering in Medicine and Biology Society (EMBC)*, 2015, pp. 3101–3104.
- [73] B. Potočník and D. Zazula, "Automated analysis of a sequence of ovarian ultrasound images. Part I: Segmentation of single 2D images," *Image Vis. Comput.*, vol. 20, no. 3, pp. 217–225, 2002.
- [74] F. Destrepes, M.-H. R. Cardinal, L. Allard, J.-C. Tardif, G. Cloutier, and M.-H. Roy Cardinal, "Segmentation method of intravascular ultrasound images of human coronary arteries," *Comput. Med. Imaging Graph.*, vol. 38, pp. 1–13, 2013.
- [75] J. Yan and Y. Cui, "A novel approach for segmentation of intravascular ultrasound images," in *Bioelectronics and Bioinformatics (ISBB), 2015 International Symposium on*, 2015, pp. 51–54.
- [76] G. Ponomarev, M. Gelfand, and M. Kazanov, "A multilevel thresholding combined with edge detection and shape-based recognition for segmentation of fetal ultrasound images," in *Proceedings of Challenge US: Biometric Measurements from Fetal Ultrasound Images, ISBI 2012 (2012)*, 2012, pp. 17–19.
- [77] I. Wendelhag, Q. Liang, T. Gustavsson, and J. Wikstrand, "A new automated computerized analyzing system simplifies readings and reduces the variability in ultrasound measurement of intima-media thickness," *Stroke*, vol. 28, no. 11, pp. 2195–2200, 1997.

- [78] S. Timp and N. Karssemeijer, "A new 2D segmentation method based on dynamic programming applied to computer aided detection in mammography.," *Med. Phys.*, vol. 31, no. 2004, pp. 958–971, 2004.
- [79] G. Zahnd, K. Kapellas, M. van Hattem, A. van Dijk, A. Sérusclat, P. Moulin, A. van der Lugt, M. Skilton, and M. Orkisz, "A fully-automatic method to segment the carotid artery layers in ultrasound imaging: application to quantify the compression-decompression pattern of the intima-media complex during the cardiac cycle," *Ultrasound Med. Biol.*, vol. 43, no. 1, pp. 239–257, 2017.
- [80] P. Hough, "Method and means for recognizing complex patterns," 1962.
- [81] S. Golemati, J. Stoitsis, E. G. Sifakis, T. Balkizas, and K. S. Nikita, "Using the Hough transform to segment ultrasound images of longitudinal and transverse sections of the carotid artery," *Ultrasound Med. Biol.*, vol. 33, no. 12, pp. 1918–1932, 2007.
- [82] Y. Zhou, Y.-P. Zheng, and Y. Zheng, "estimation of muscle fiber orientation in ultrasound images using revoting Hough transform (RVHT)," *Ultrasound Med. Biol.*, vol. 34, no. 9, pp. 1474–1481, 2008.
- [83] S. Tsantis, N. Dimitropoulos, D. Cavouras, and G. Nikiforidis, "A hybrid multi-scale model for thyroid nodule boundary detection on ultrasound images," *Comput. Methods Programs Biomed.*, vol. 84, no. 2, pp. 86–98, 2006.
- [84] X. Liu, J. Yu, Y. Wang, and P. Chen, "Automatic localization of the fetal cerebellum on 3D ultrasound volumes," *Med. Phys.*, vol. 40, no. 11, p. 112902, 2013.
- [85] Y. Zhu, X. Papademetris, A. J. Sinusas, and J. S. Duncan, "A coupled deformable model for tracking myocardial borders from real-time echocardiography using an incompressibility constraint," *Med. Image Anal.*, vol. 14, no. 3, pp. 429–448, 2010.
- [86] T. Tan, B. Platel, R. M. Mann, H. Huisman, and N. Karssemeijer, "Chest wall segmentation in automated 3D breast ultrasound scans," *Med. Image Anal.*, vol. 17, no. 8, pp. 1273–1281, 2013.
- [87] A. Wong, K. M. Gallagher, and J. P. Callaghan, "Computerised system for measurement of muscle thickness based on ultrasonography," *Comput. Methods Biomech. Biomed. Engin.*, vol. 16, no. 3, pp. 1–7, 2012.
- [88] P. Han, Y. Chen, L. Ao, G. Xie, H. Li, L. Wang, and Y. Zhou, "Automatic thickness estimation for skeletal muscle in ultrasonography: evaluation of two enhancement methods.," *Biomed. Eng. Online*, vol. 12, p. 6, 2013.
- [89] Q. Li, S. Qi, H. Zhang, Y. Deng, X. Chen, S. Chen, and T. Wang, "Continuous thickness measurement of rectus femoris muscle in ultrasound image sequences: A completely automated approach," *Biomed. Signal Process. Control*, vol. 8, no. 6, pp. 792–798, 2013.
- [90] H. F. García, J. J. Giraldo, M. A. Alvarez, A. A. Orozco, and D. Salazar, "Peripheral nerve segmentation using speckle removal and Bayesian shape models," in *Iberian Conference on Pattern Recognition and Image Analysis*, 2015, pp. 387–394.
- [91] L. Xiao, Q. Li, Y. Bai, L. Zhang, and J. Tang, "Automated measurement method of common carotid artery intima-media thickness in ultrasound image based on Markov random field models," *J. Med. Biol. Eng.*, vol. 35, no. 5, pp. 651–660, Oct. 2015.
- [92] W. M. A. N. M. Hafizah and E. K. O. Supriyanto, "Automatic region of interest generation for kidney ultrasound images," *Proceeding Recent Res. Appl. Informatics Remote Sens.*, pp. 70–75, 2011.
- [93] A. Gupta, M. Tech, B. Gosain, B. Tech, and S. Kaushal, "A comparison of two algorithms for

automated stone detection in clinical B-mode ultrasound images of the abdomen,” *J. Clin. Monit. Comput.*, vol. 24, no. 5, pp. 341–362, 2010.

- [94] S. Rosati, G. Balestra, F. Molinari, U. Rajendra Acharya, and J. Suri, “A selection and reduction approach for the optimization of ultrasound carotid artery images segmentation,” in *Machine Learning in Healthcare Informatics SE - 14*, vol. 56, S. Dua, U. R. Acharya, and P. Dua, Eds. Springer Berlin Heidelberg, 2014, pp. 309–332.
- [95] D. Bibicu, L. Moraru, and A. Biswas, “Thyroid nodule recognition based on feature selection and pixel classification methods,” *J. Digit. Imaging*, vol. 26, no. 1, pp. 119–128, 2012.
- [96] R.-M. Menchón-Lara, J.-L. Sancho-Gómez, and A. Bueno-Crespo, “Early-stage atherosclerosis detection using deep learning over carotid ultrasound images,” *Appl. Soft Comput.*, vol. 49, pp. 616–628, 2016.
- [97] E. Keramidas, D. Iakovidis, D. Maroulis, and N. Dimitropoulos, “Automatic measurement of thyroid gland,” in *Panhellenic Conference on Informatics (PCI 2007)*, 2007, pp. 49–56.
- [98] C. Caresio, M. Salvi, F. Molinari, K. M. Meiburger, and M. A. Minetto, “Fully automated muscle ultrasound analysis (MUSA): robust and accurate muscle thickness measurement,” *Ultrasound Med. Biol.*, vol. 43, no. 1, pp. 195–205, 2017.
- [99] R.-M. Menchón-Lara, J.-L. Sancho-Gómez, and A. Bueno-Crespo, “Early-stage atherosclerosis detection using deep learning over carotid ultrasound images,” *Appl. Soft Comput.*, vol. 49, pp. 616–628, 2016.
- [100] I. Wendelhag, T. Gustavsson, M. Suurkula, G. Berglund, and J. Wikstrand, “Ultrasound measurement of wall thickness in the carotid artery: fundamental principles and description of a computerized analysing system,” *Clin. Physiol.*, vol. 11, no. 6, pp. 565–77, Nov. 1991.
- [101] I. Wendelhag, Q. Liang, T. Gustavsson, and J. Wikstrand, “A new automated computerized analyzing system simplifies readings and reduces the variability in ultrasound measurement of intima-media thickness,” *Stroke*, vol. 28, no. 11, pp. 2195–200, Nov. 1997.
- [102] X. Liu, J. Yu, Y. Wang, and P. Chen, “Automatic localization of the fetal cerebellum on 3D ultrasound volumes,” *Med. Phys.*, vol. 40, no. 11, p. 112902, 2013.
- [103] G. Pons, J. Martí, R. Martí, S. Ganau, J. C. Vilanova, and J. A. Noble, “Evaluating Lesion Segmentation on Breast Sonography as Related to Lesion Type,” *J. Ultrasound Med.*, vol. 32, no. 9, pp. 1659–1670, Sep. 2013.
- [104] M. Xian, J. Huang, Y. Zhang, and X. Tang, “Multiple-domain knowledge based MRF model for tumor segmentation in breast ultrasound images,” in *2012 19th IEEE International Conference on Image Processing*, 2012, pp. 2021–2024.
- [105] A. Takemura, A. Shimizu, and K. Hamamoto, “A cost-sensitive extension of AdaBoost with markov random field priors for automated segmentation of breast tumors in ultrasonic images,” *Int. J. Comput. Assist. Radiol. Surg.*, vol. 5, no. 5, pp. 537–547, Sep. 2010.
- [106] Zhong Tao, H. D. Tagare, and J. D. Beaty, “Evaluation of four probability distribution models for speckle in clinical cardiac ultrasound images,” *IEEE Trans. Med. Imaging*, vol. 25, no. 11, pp. 1483–1491, Nov. 2006.
- [107] M. M. Nillesen, R. G. P. Lopata, I. H. Gerrits, L. Kapusta, J. M. Thijssen, and C. L. de Korte, “Modeling envelope statistics of blood and myocardium for segmentation of echocardiographic images,” *Ultrasound Med. Biol.*, vol. 34, no. 4, pp. 674–680, 2008.

- [108] Y. Xu, T. Mo, Q. Feng, P. Zhong, M. Lai, and E. I.-C. Chang, "Deep learning of feature representation with multiple instance learning for medical image analysis," in *2014 IEEE International Conference on Acoustics, Speech and Signal Processing (ICASSP)*, 2014, pp. 1626–1630.
- [109] Y. LeCun, Y. Bengio, and G. Hinton, "Deep learning," *Nature*, vol. 521, no. 7553, pp. 436–444, May 2015.
- [110] J. H. Tan, U. R. Acharya, S. V. Bhandary, K. C. Chua, and S. Sivaprasad, "Segmentation of optic disc, fovea and retinal vasculature using a single convolutional neural network," *J. Comput. Sci.*, vol. 20, pp. 70–79, 2017.
- [111] J. H. Tan, H. Fujita, S. Sivaprasad, S. V. Bhandary, A. K. Rao, K. C. Chua, and U. R. Acharya, "Automated segmentation of exudates, haemorrhages, microaneurysms using single convolutional neural network," *Inf. Sci. (Ny)*, vol. 420, pp. 66–76, Dec. 2017.
- [112] F. C. Ghesu, E. Krubasik, B. Georgescu, and V. Singh, "Marginal space deep learning : efficient architecture for volumetric image parsing," *IEEE Trans. Med. Imaging*, vol. 35, no. 5, pp. 1217–1228, 2016.
- [113] G. Carneiro, J. C. Nascimento, and A. Freitas, "The segmentation of the left ventricle of the heart from ultrasound data using deep learning architectures and derivative-based search methods," *IEEE Trans. Image Process.*, vol. 21, no. 3, pp. 968–982, 2012.
- [114] P. Sermanet and D. Eigen, "OverFeat : integrated recognition, localization and detection using convolutional networks," *arXiv Prepr. arXiv*, vol. 1312, no. 6229, 2013.
- [115] A. Krizhevsky, I. Sutskever, and G. E. Hinton, "ImageNet classification with deep convolutional neural networks," in *Advances in neural information processing systems*, 2012, pp. 1097–1105.
- [116] F. Milletari, S. Ahmadi, C. Kroll, A. Plate, V. Rozanski, J. Maiostre, J. Levin, O. Dietrich, B. Ertl-wagner, K. Bötzel, and N. Navab, "Hough-CNN : Deep learning for segmentation of deep brain regions in MRI and ultrasound," *Comput. Vis. Image Underst.*, vol. 0, pp. 1–11, 2017.
- [117] J. J. Cerrolaza, N. Safdar, E. Biggs, J. Jago, C. A. Peters, and M. G. Linguraru, "Renal Segmentation from 3D Ultrasound via Fuzzy Appearance Models and Patient-Specific Alpha Shapes," *IEEE Trans. Med. Imaging*, vol. 35, no. 11, pp. 2393–2402, 2016.
- [118] H. Ravishankar, P. Annangi, M. Washburn, and J. Lanning, "Automated kidney morphology measurements from ultrasound images using texture and edge analysis," *SPIE Med. Imaging. Int. Soc. Opt. Photonics*, vol. 9790, no. April 2016, p. 97901A, 2016.
- [119] E. H. Chang, W. K. Chong, S. K. Kasoji, J. R. Fielding, E. Altun, L. B. Mullin, J. I. Kim, J. P. Fine, P. A. Dayton, and W. K. Rathmell, "Diagnostic accuracy of contrast-enhanced ultrasound for characterization of kidney lesions in patients with and without chronic kidney disease," *BMC Nephrol.*, vol. 18, no. 1, p. 266, 2017.
- [120] T. Mangayarkarasi and D. N. Jamal, "PNN-based analysis system to classify renal pathologies in Kidney Ultrasound Images," *Proc. 2017 2nd Int. Conf. Comput. Commun. Technol. ICCCT 2017*, pp. 123–126, 2017.
- [121] K. Bommanna Raja, M. Madheswaran, and K. Thyagarajah, "A hybrid fuzzy-neural system for computer-aided diagnosis of ultrasound kidney images using prominent features," *J. Med. Syst.*, vol. 32, no. 1, pp. 65–83, 2008.
- [122] L. Li, P. Ross, M. Kruusmaa, and X. Zheng, "A comparative study of ultrasound image segmentation algorithms for segmenting kidney tumors," *Proc. 4th Int. Symp. Appl. Sci. Biomed. Commun. Technol.*

- ISABEL '11, pp. 1–5, 2011.

- [123] G. Slabaugh, G. Unal, M. Wels, T. Fang, and B. Rao, "Statistical region-based segmentation of ultrasound images," *Ultrasound Med. Biol.*, 2009.
- [124] M. Martín-Fernández and C. Alberola-Lopez, "An approach for contour detection of human kidneys from ultrasound images using Markov random fields and active contours," *Med. Image Anal.*, vol. 9, no. 1, pp. 1–23, 2005.
- [125] C. Chen, H. Lu, and K. Han, "A textural approach based on Gabor functions for texture edge detection in ultrasound images," *Ultrasound Med. Biol.*, vol. 27, no. 4, pp. 515–534, 2001.
- [126] T. Chan and L. Vese, "Active contours without edges," *IEEE Trans. image Process.*, vol. 10, no. 2, pp. 266–277, 2001.
- [127] M. Cvancarova, F. Albregtsen, and K. Brabrand, "Segmentation of ultrasound images of liver tumors applying snake algorithms and GVF," in *International Congress Series*, 2005, pp. 218–223.
- [128] V. Velmurugan, M. Arunkimar, and P. Gnanasivam, "A Review on Systemic Approach of the Ultra Sound Image to Detect Renal Calculi Using Different Analysis Techniques," in *International Conference on Biosignals, images and instrumentation*, 2017, no. March 16-18.
- [129] J. Verma, M. Nath, P. Tripathi, and K. K. Saini, "Analysis and identification of kidney stone using Kth nearest neighbour (KNN) and support vector machine (SVM) classification techniques," *Pattern Recognit. Image Anal.*, vol. 27, no. 3, pp. 574–580, 2017.
- [130] P. R. Tamilselvi and P. Thangaraj, "Computer aided diagnosis system for stone detection and early detection of kidney stones," *J. Comput. Sci.*, vol. 7, no. 2, pp. 250–254, 2011.
- [131] A. Jalalian, S. B. T. Mashohor, H. R. Mahmud, M. I. B. Saripan, A. R. B. Ramli, and B. Karasfi, "Computer-aided detection/diagnosis of breast cancer in mammography and ultrasound: A review," *Clin. Imaging*, vol. 37, no. 3, pp. 420–426, 2013.
- [132] B. Sahiner, H. Chan, M. Roubidoux, and L. Hadjiiski, "Malignant and benign breast masses on 3D US volumetric images: effect of computer-aided diagnosis on radiologist accuracy," *Radiology*, vol. 242, no. 3, pp. 716–724, 2007.
- [133] C. Chen, Y. Chou, K. Han, G. Hung, and C. Tiu, "Breast lesions on sonograms: Computer-aided diagnosis with nearly setting-independent features and artificial neural networks," *Radiology*, vol. 226, no. 2, pp. 504–514, 2003.
- [134] H. Teixidor and E. Kazam, "Combined mammographic-sonographic evaluation of breast masses," *Am. J. Roentgenol.*, vol. 128, no. 3, pp. 409–417, 1977.
- [135] C. Lo, R. Chen, Y. Chang, Y. Yang, M. Hung, C. Huang, and R. Chang, "Multi-dimensional tumor detection in automated whole breast ultrasound using topographic watershed," *IEEE Trans Med Imaging*, vol. 33, no. 7, pp. 1503–1511, 2014.
- [136] Q. Huang, Y. Luo, and Q. Zhang, "Breast ultrasound image segmentation: a survey," *Int. J. Comput. Assist. Radiol. Surg.*, vol. 12, no. 3, pp. 493–507, Mar. 2017.
- [137] J. Shan, H. D. Cheng, and Y. Wang, "Completely Automated Segmentation Approach for Breast Ultrasound Images Using Multiple-Domain Features," *Ultrasound Med. Biol.*, vol. 38, no. 2, pp. 262–275, Feb. 2012.
- [138] J. Shan, H. D. Cheng, and Y. Wang, "A novel segmentation method for breast ultrasound images

based on neutrosophic l-means clustering," *Med. Phys.*, vol. 39, no. 9, pp. 5669–5682, Aug. 2012.

- [139] T. Tan, B. Platel, R. Mus, and L. Tabar, "Computer-aided detection of cancer in automated 3-D breast ultrasound," *IEEE Trans. Med. Imaging*, vol. 32, no. 9, pp. 1698–1706, 2013.
- [140] W. Moon, Y. Shen, and M. Bae, "Computer-aided tumor detection based on multi-scale blob detection algorithm in automated breast ultrasound images," *IEEE Trans. Med. Imaging*, vol. 32, no. 7, pp. 1191–1200, 2013.
- [141] Y. Ikeda, D. Fukuoka, T. Hara, H. Fujita, and E. Takada, "Development of a fully automatic scheme for detection of masses in whole breast ultrasound images," *Med. Phys.*, vol. 34, no. 11, pp. 4378–4388, 2007.
- [142] R. Chang, K. Chang-Chien, and E. Takada, "Rapid image stitching and computer-aided detection for multipass automated breast ultrasound," *Med. Phys.*, vol. 37, no. 5, pp. 2063–2073, 2010.
- [143] R. Chang, K. Chang-Chien, and H. Chen, "Whole breast computer-aided screening using free-hand ultrasound," in *International Congress Series*, 2005, vol. 1281, pp. 1075–1080.
- [144] T. Tan, B. Platel, R. Mus, L. Tabar, R. M. Mann, and N. Karssemeijer, "Computer-aided detection of cancer in automated 3-D breast ultrasound," *IEEE Trans. Med. Imaging*, vol. 32, no. 9, pp. 1698–1706, 2013.
- [145] V. Tavakoli and A. A. Amini, "A survey of shaped-based registration and segmentation techniques for cardiac images," *Comput. Vis. Image Underst.*, vol. 117, no. 9, pp. 966–989, 2013.
- [146] T. Mäkelä, P. Clarysse, O. Sipilä, and N. Pauna, "A review of cardiac image registration methods," *IEEE Trans. Med. Imaging*, vol. 21, no. 9, pp. 1011–1021, 2002.
- [147] A. Frangi and W. Niessen, "Three-dimensional modeling for functional analysis of cardiac images, a review," *IEEE Trans. Med. Imaging*, vol. 20, no. 1, pp. 2–5, 2001.
- [148] L. L. Valsangiacomo Buechel, Emanuela R., Mertens, "Imaging the right heart: the use of integrated multimodality imaging," *Eur. Heart J.*, vol. 33, no. 8, pp. 949–960, 2012.
- [149] L. L. Mertens and M. K. Friedberg, "Imaging the right ventricle—current state of the art," *Nat. Rev. Cardiol.*, vol. 7, no. 10, pp. 551–563, Oct. 2010.
- [150] T. Binder, M. Süssner, D. Moertl, T. Strohmer, H. Baumgartner, G. Maurer, and G. Porenta, "Artificial neural networks and spatial temporal contour linking for automated endocardial contour detection on echocardiograms: a novel approach to determine left ventricular contractile function," *Ultrasound Med. Biol.*, vol. 25, no. 7, pp. 1069–1076, 1999.
- [151] C. Rekeczky, Á. Tahy, Z. Végh, and T. Roska, "CNN-based spatio-temporal nonlinear filtering and endocardial boundary detection in echocardiography," *Int. J. Circuit Theory Appl.*, vol. 27, no. 1, pp. 171–207, 1999.
- [152] Guofang Xiao, M. Brady, J. A. Noble, and Yongyue Zhang, "Segmentation of ultrasound B-mode images with intensity inhomogeneity correction," *IEEE Trans. Med. Imaging*, vol. 21, no. 1, pp. 48–57, 2002.
- [153] Y. Chen, F. Huang, and M. Rao, "Using prior shape and intensity profile in medical image segmentation," in *IEEE International Conference on Computer Vision*, 2003, pp. 1117–1124.
- [154] Y. Chen, F. Huang, H. Tagare, and M. Rao, "A coupled minimization problem for medical image segmentation with priors," *Int. J. Comput. Vis.*, vol. 71, no. 3, pp. 259–272, 2007.

- [155] J. Yan and T. Zhuang, "Applying improved fast marching method to endocardial boundary detection in echocardiographic images," *Pattern Recognit. Lett.*, vol. 24, no. 15, pp. 2777–2784, 2003.
- [156] M. Mignotte and J. Meunier, "A multiscale optimization approach for the dynamic contour-based boundary detection issue," *Comput. Med. Imaging Graph.*, vol. 25, no. 3, pp. 265–275, 2001.
- [157] P. Yan, A. Sinusas, and J. S. Duncan, "Boundary element method-based regularization for recovering of LV deformation," *Med. Image Anal.*, vol. 11, no. 6, pp. 540–554, Dec. 2007.
- [158] D. Koundal, "Computer-aided diagnosis of thyroid nodule: a review," *Int. J. Comput. Sci. Eng. Surv.*, vol. 3, no. 4, pp. 67–83, 2012.
- [159] T. Wunderling, B. Golla, P. Poudel, C. Arens, M. Friebe, and C. Hansen, "Comparison of thyroid segmentation techniques for 3D ultrasound," in *SPIE Medical Imaging*, 2017, vol. 1013317, no. February, p. 1013317.
- [160] R. Z. Slapa, W. S. Jakubowski, J. Slowinska-Srzednicka, and K. T. Szopinski, "Advantages and disadvantages of 3D ultrasound of thyroid nodules including thin slice volume rendering.," *Thyroid Res.*, vol. 4, no. 1, p. 1, 2011.
- [161] S. C. Kim, J.-H. Kim, S. H. Choi, T. J. Yun, J. Y. Wi, S. A. Kim, H. Y. Sun, I. Ryoo, S.-W. Park, and C.-H. Sohn, "Off-site evaluation of three-dimensional ultrasound for the diagnosis of thyroid nodules: comparison with two-dimensional ultrasound.," *Eur. Radiol.*, vol. 26, no. 10, pp. 3353–3360, 2016.
- [162] W. Xin and X. Wen-Jie, "Fusion Kernel Fuzzy C-Means Clustering and Improved Distance Regularized Level Set Evolution Model of Thyroid Nodules Segmentation," *J. Med. Imaging Heal. Informatics*, vol. 6, no. 5, pp. 1330–1336, 2016.
- [163] D. Koundal, S. Gupta, and S. Singh, "Computer aided thyroid nodule detection system using medical ultrasound images," *Biomed. Signal Process. Control*, vol. 40, pp. 117–130, 2018.
- [164] Y. Chang, A. K. Paul, N. Kim, J. H. Baek, Y. J. Choi, E. J. Ha, K. D. Lee, H. S. Lee, D. Shin, and N. Kim, "Computer-aided diagnosis for classifying benign versus malignant thyroid nodules based on ultrasound images: A comparison with radiologist-based assessments," *Med. Phys.*, vol. 43, no. 1, pp. 554–567, 2016.
- [165] M. A. Savelonas, D. K. Iakovidis, I. Legakis, and D. Maroulis, "Active contours guided by echogenicity and texture for delineation of thyroid nodules in ultrasound images," *IEEE Trans. Inf. Technol. Biomed.*, vol. 13, no. 4, pp. 519–527, 2009.
- [166] J. Virmani, V. Kumar, and N. Kalra, "Neural network ensemble based CAD system for focal liver lesions from B-mode ultrasound," *J. Digit. Imaging*, vol. 24, no. 4, pp. 520–537, 2014.
- [167] U. R. Acharya, O. Faust, F. Molinari, S. V. Sree, S. P. Junnarkar, and V. Sudarshan, "Ultrasound-based tissue characterization and classification of fatty liver disease: A screening and diagnostic paradigm," *Knowledge-Based Syst.*, vol. 75, pp. 66–77, Feb. 2015.
- [168] H. Zhu, J. Sheng, F. Zhang, J. Zhou, and J. Wang, "Improved maximally stable extremal regions based method for the segmentation of ultrasonic liver images," *Ultim. Tools Appl.*, vol. 75, no. 18, pp. 10979–10997, 2016.
- [169] H. Zhu, Z. Zhuang, J. Zhou, F. Zhang, X. Wang, and Y. Wu, "Segmentation of liver cyst in ultrasound image based on adaptive threshold algorithm and particle swarm optimization," *Multimed. Tools Appl.*, vol. 76, no. 6, pp. 1–18, Apr. 2016.
- [170] N. Jain and V. Kumar, "Liver Ultrasound Image Segmentation Using Region-Difference Filters," *J.*

Digit. Imaging, vol. 30, no. 3, pp. 376–390, 2017.

- [171] E. Ukwatta, J. Yuan, D. Buchanan, B. Chiu, J. Awad, W. Qiu, G. Parraga, and A. Fenster, “Three-dimensional segmentation of three-dimensional ultrasound carotid atherosclerosis using sparse field level sets,” *Med. Phys.*, vol. 40, no. 5, 2013.
- [172] F. Destrempes, J. Meunier, M. F. Giroux, G. Soulez, and G. Cloutier, “Segmentation of plaques in sequences of ultrasonic B-mode images of carotid arteries based on motion estimation and a Bayesian model,” *IEEE Trans. Biomed. Eng.*, vol. 58, no. 8, pp. 2202–2211, Aug. 2011.
- [173] S. Delsanto, F. Molinari, P. Giustetto, W. Liboni, S. Badalamenti, and J. S. Suri, “Characterization of a completely user-independent algorithm for carotid artery segmentation in 2-D ultrasound images,” *IEEE Trans. Instrum. Meas.*, vol. 56, no. 4, pp. 1265–1274, 2007.
- [174] P. . Shankar, F. Forsberg, and L. Lown, “Statistical modeling of atherosclerotic plaque in carotid B mode images—a feasibility study,” *Ultrasound Med. Biol.*, vol. 29, no. 9, pp. 1305–1309, 2003.
- [175] C. I. Christodoulou, C. S. Pattichis, M. Pantziaris, and A. Nicolaides, “Texture-based classification of atherosclerotic carotid plaques,” *IEEE Trans. Med. Imaging*, vol. 22, no. 7, pp. 902–912, Jul. 2003.
- [176] B. K. Lal, R. W. Hobson, P. J. Pappas, R. Kubicka, M. Hameed, E. Y. Chakhtura, Z. Jamil, F. T. Padberg, P. B. Haser, and W. N. Durán, “Pixel distribution analysis of B-mode ultrasound scan images predicts histologic features of atherosclerotic carotid plaques,” *J. Vasc. Surg.*, vol. 35, no. 6, pp. 1210–1217, 2002.
- [177] F. Molinari, W. Liboni, E. Pavanelli, P. Giustetto, S. Badalamenti, and J. S. Suri, “Accurate and automatic carotid plaque characterization in contrast enhanced 2-D ultrasound images,” in *2007 29th Annual International Conference of the IEEE Engineering in Medicine and Biology Society*, 2007, pp. 335–338.
- [178] U. R. Acharya, O. Faust, S. V. Sree, F. Molinari, L. Saba, A. Nicolaides, and J. S. Suri, “An accurate and generalized approach to plaque characterization in 346 carotid ultrasound scans,” *IEEE Trans. Instrum. Meas.*, vol. 61, no. 4, pp. 1045–1053, Apr. 2012.
- [179] U. R. Acharya, S. V. Sree, M. M. R. Krishnan, F. Molinari, L. Saba, S. Y. S. Ho, A. T. Ahuja, S. C. Ho, A. Nicolaides, and J. S. Suri, “Atherosclerotic Risk Stratification Strategy for Carotid Arteries Using Texture-Based Features,” *Ultrasound Med. Biol.*, vol. 38, no. 6, pp. 899–915, Jun. 2012.
- [180] A. Fenster, G. Parraga, and A. Landry, “3-D US imaging of the carotid arteries,” in *Advances in Diagnostic and Therapeutic Ultrasound Imaging*, 2008, pp. 67–92.
- [181] U. Schminke, L. Motsch, B. Griewing, M. Gaull, and C. Kessler, “Three-dimensional power-mode ultrasound for quantification of the progression of carotid artery atherosclerosis,” *J. Neurol.*, vol. 247, no. 2, pp. 106–111, Feb. 2000.
- [182] A. Troyer, D. Saloner, X. M. Pan, P. Velez, and J. H. Rapp, “Major carotid plaque surface irregularities correlate with neurologic symptoms,” *J. Vasc. Surg.*, vol. 35, no. 4, pp. 741–747, 2002.
- [183] T. Hatsukami, B. Thackray, J. Primozich, M. Ferguson, D. Burns, K. Beach, P. Detmer, C. Alpers, D. Gordon, and D. Strandness, “Echolucent regions in carotid plaque: preliminary analysis comparing three-dimensional histologic reconstructions to sonographic findings,” *Ultrasound Med. Biol.*, vol. 20, no. 8, pp. 743–749, 1994.
- [184] J. Cheng, H. Li, F. Xiao, A. Fenster, X. Zhang, X. He, L. Li, and M. Ding, “Fully automatic plaque segmentation in 3-D carotid ultrasound images,” *Ultrasound Med. Biol.*, vol. 39, no. 12, pp. 2431–2446, 2013.

- [185] A. Katouzian, E. D. Angelini, S. G. Carlier, J. S. Suri, N. Navab, and A. F. Laine, "A state-of-the-art review on segmentation algorithms in intravascular ultrasound (IVUS) images," *IEEE Trans. Inf. Technol. Biomed.*, vol. 16, no. 5, pp. 823–834, 2012.
- [186] J. A. Sethian, "A fast marching level set method for monotonically advancing fronts," *Pnas*, vol. 93, no. 4, pp. 1591–1595, 1996.
- [187] D. M. Herrington, T. Johnson, P. Santago, and W. E. Snyder, "Semi-automated boundary detection for intravascular ultrasound," *Proc. Comput. Cardiol.*, pp. 103–106, 1992.
- [188] M. Sonka, X. Zhang, M. Siebes, M. S. Bissing, S. C. Dejong, S. M. Collins, and C. R. McKay, "Segmentation of intravascular ultrasound images: a knowledge-based approach," *IEEE Trans. Med. Imaging*, vol. 14, no. 4, pp. 719–32, 1995.
- [189] a. H. Hernandez, D. G. Gil, P. R. Radeva, and E. N. Nofrerias, "Anisotropic processing of image structures for adventitia detection in intravascular ultrasound images," *Comput. Cardiol. 2004*, pp. 229–232, 2004.
- [190] E. Brusseau, C. L. De Korte, F. Mastik, J. Schaar, and A. F. W. Van Der Steen, "Fully Automatic Luminal Contour Segmentation in Intracoronary Ultrasound Imaging — A Statistical Approach," *IEEE Trans. Med. Imaging*, vol. 23, no. 5, pp. 554–566, 2004.
- [191] M.-H. R. Cardinal, J. Meunier, G. Soulez, R. L. Maurice, E. Therasse, and G. Cloutier, "Intravascular ultrasound image segmentation: a three-dimensional fast-marching method based on gray level distributions," *IEEE Trans. Med. Imaging*, vol. 25, no. 5, pp. 590–601, 2006.
- [192] A. Katouzian, B. Baseri, E. E. Konofagou, and A. F. Laine, "Automatic detection of blood versus non-blood regions on intravascular ultrasound (IVUS) images using wavelet packet signatures," in *SPIE Medical Imaging*, 2008, no. March 2008, p. 69200H–1–69200H–8.
- [193] A. Simon, J. Garipey, G. Chironi, J. Megnien, and J. Levenson, "Intima–media thickness: a new tool for diagnosis and treatment of cardiovascular risk," *J. Hypertens.*, vol. 20, no. 2, pp. 159–69, 2002.
- [194] C. P. Loizou, "A review of ultrasound common carotid artery image and video segmentation techniques," *Med. Biol. Eng. Comput.*, vol. 52, no. 12, pp. 1073–1093, 2014.
- [195] R. Rocha, A. Campilho, J. Silva, E. Azevedo, and R. Santos, "Segmentation of the carotid intima-media region in B-Mode ultrasound images," *Image Vis. Comput.*, vol. 28, no. 4, pp. 614–625, 2010.
- [196] R. Rocha, A. Campilho, J. Silva, E. Azevedo, and R. Santos, "Segmentation of ultrasound images of the carotid using RANSAC and cubic splines," *Comput Methods Programs Biomed*, vol. 101, pp. 94–106, 2011.
- [197] G. Zahnd, K. Kapellas, M. Van Hattem, and A. Van Dijk, "A Fully-Automatic Method to Segment the Carotid Artery Layers in Ultrasound Imaging: Application to Quantify the Compression-Decompression Pattern of the Intima-," *Ultrasound Med. Biol.*, vol. 43, no. 1, pp. 239–257, 2017.
- [198] L. Xiao, Q. Li, Y. Bai, L. Zhang, and J. Tang, "Automated Measurement Method of Common Carotid Artery Intima-Media Thickness in Ultrasound Image Based on Markov Random Field Models," *J. Med. Biol. Eng.*, vol. 35, no. 5, pp. 651–660, Oct. 2015.
- [199] P. Touboul, M. Hennerici, S. Meairs, and H. Adams, "Mannheim carotid intima-media thickness and plaque consensus (2004–2006–2011)," *Cerebrovasc. Dis.*, vol. 34, no. 4, pp. 290–296, 2012.
- [200] N. Ikeda, N. Dey, A. Sharma, A. Gupta, S. Bose, S. Acharjee, S. Shafique, E. Cuadrado-Godia, T. Araki, L. Saba, J. R. Laird, A. Nicolaidis, and J. S. Suri, "Automated segmental-IMT measurement in

thin/thick plaque with bulb presence in carotid ultrasound from multiple scanners: Stroke risk assessment,” *Comput. Methods Programs Biomed.*, vol. 141, pp. 73–81, Apr. 2017.

- [201] F. Molinari, G. Zeng, and J. S. Suri, “An integrated approach to computer-based automated tracing and its validation for 200 common carotid arterial wall ultrasound images: a new technique,” *J. Ultrasound Med.*, vol. 29, no. 3, pp. 399–418, 2010.
- [202] M. Narici, C. Maganaris, and N. Reeves, “Effect of aging on human muscle architecture,” *J. Appl.*, vol. 95, no. 6, pp. 2229–2234, 2003.
- [203] M. Narici, M. Flueck, and A. Koesters, “Skeletal muscle remodeling in response to alpine skiing training in older individuals,” *Scand. J. Med. Sci. Sports*, vol. 21, no. s1, pp. 23–28, 2011.
- [204] O. Seynnes, S. Kamandulis, and R. Kairaitis, “Effect of androgenic-anabolic steroids and heavy strength training on patellar tendon morphological and mechanical properties,” *J. Appl. Physiol.*, vol. 115, no. 1, pp. 84–89, 2013.
- [205] M. de Boer, O. Seynnes, and P. Di Prampero, “Effect of 5 weeks horizontal bed rest on human muscle thickness and architecture of weight bearing and non-weight bearing muscles,” *Eur. J. Appl. Physiol.*, vol. 104, no. 2, pp. 401–407, 2008.
- [206] R. Atkinson, “Effects of testosterone on skeletal muscle architecture in intermediate-frail and frail elderly men,” *Journals Gerontol. Ser. A Biomed. Sci. Med. Sci.*, vol. 65, no. 11, pp. 1215–1219, 2010.
- [207] S. Agyapong-Badu, M. Warner, and D. Samuel, “Anterior thigh composition measured using ultrasound imaging to quantify relative thickness of muscle and non-contractile tissue: a potential biomarker for musculoskeletal health,” *Physiol. Meas.*, vol. 35, no. 10, p. 2165, 2014.
- [208] S. Pillen, I. Arts, and M. Zwarts, “Muscle ultrasound in neuromuscular disorders,” *Muscle Nerve*, vol. 37, no. 6, pp. 679–693, 2008.
- [209] X. Chen, Q. Li, S. Qi, H. Zhang, S. Chen, and T. Wang, “Continuous fascicle orientation measurement of medial gastrocnemius muscle in ultrasonography using frequency domain Radon transform,” *Biomed. Signal Process. Control*, vol. 20, pp. 117–124, 2015.
- [210] J. Gillett, R. Barrett, and G. Lichtwark, “Reliability and accuracy of an automated tracking algorithm to measure controlled passive and active muscle fascicle length changes from ultrasound,” *Comput. Methods Biomech. Biomed. Engin.*, vol. 16, no. 6, pp. 678–687, 2013.
- [211] N. J. Cronin, C. P. Carty, R. S. Barrett, G. Lichtwark, N. Aggeloussis, E. Giannakou, K. Albracht, A. Arampatzis, S. Baker, I. Matthews, M. Benard, J. Becher, J. Harlaar, P. Huijing, R. Jaspers, T. Besier, D. Sturnieks, J. Alderson, D. Lloyd, J. Bojsen-Moller, P. Hansen, P. Aagaard, U. Svantesson, M. Kjaer, S. Magnusson, N. Cronin, R. af Klint, M. Grey, T. Sinkjaer, N. Cronin, J. Peltonen, M. Ishikawa, P. Komi, J. Avela, T. Sinkjaer, M. Voigt, S. Delp, F. Anderson, A. Arnold, P. Loan, A. Habib, C. John, E. Guendelman, D. Thelen, S. Delp, J. Loan, M. Hoy, F. Zajac, E. Topp, J. Rosen, A. Ferrari, A. Cutti, A. Cappello, T. Fukunaga, K. Kubo, Y. Kawakami, S. Fukashiro, H. Kanehisa, C. Maganaris, R. Griffiths, R. Griffiths, S. Hamner, A. Seth, S. Delp, J. Hoffer, A. Caputi, I. Pose, R. Griffiths, M. Kadaba, H. Ramakrishnan, M. Wootten, J. Gainey, G. Gorton, G. Cochran, M. Klimstra, J. Dowling, J. Durkin, M. MacDonald, K. Kubo, H. Kanehisa, T. Fukunaga, G. Lichtwark, K. Bougoulas, A. Wilson, G. Lichtwark, A. Wilson, G. Lichtwark, A. Wilson, I. Loram, C. Maganaris, M. Lakie, B. Lucas, T. Kanade, S. Magnusson, P. Hansen, P. Aagaard, J. Brond, P. Dyhre-Poulsen, J. Bojsen-Moller, M. Kjaer, O. Mian, J. Thom, L. Ardigo, A. Minetti, M. Narici, T. Miyoshi, T. Kihara, H. Koyama, S. Yamamoto, T. Komeda, T. Muramatsu, T. Muraoka, Y. Kawakami, A. Shibayama, T. Fukunaga, M. Rana, G. Hamarneh, J. Wakeling, J. Van Leeuwen, C. Spoor, and D. Young, “Automatic tracking of medial gastrocnemius fascicle length during human locomotion,” *J. Appl. Physiol.*, vol. 111, no. 5, pp. 1491–6, Nov. 2011.

- [212] Y. Zhou, J.-Z. Li, G. Zhou, and Y.-P. Zheng, "Dynamic measurement of pennation angle of gastrocnemius muscles during contractions based on ultrasound imaging," *Biomed. Eng. Online*, vol. 11, no. 1, p. 63, 2012.
- [213] M. Rana, G. Hamarneh, and J. M. Wakeling, "Automated tracking of muscle fascicle orientation in B-mode ultrasound images," *J. Biomech.*, vol. 42, no. 13, pp. 2068–2073, 2009.
- [214] H. Zhao and L. Zhang, "Automatic tracking of muscle fascicles in ultrasound images using localized Radon transform," *IEEE Trans. Biomed. Eng.*, vol. 58, no. 7, pp. 2094–2101, 2011.
- [215] A. Faisal, S. C. Ng, S. L. Goh, J. George, E. Supriyanto, and K. W. Lai, "Multiple LREK active contours for knee meniscus ultrasound image segmentation," *IEEE Trans. Med. Imaging*, vol. 34, no. 10, pp. 2162–2171, 2015.
- [216] A. Hafiane, P. Vieyres, and A. Delbos, "Phase-based probabilistic active contour for nerve detection in ultrasound images for regional anesthesia," *Comput. Biol. Med.*, vol. 52, pp. 88–95, 2014.
- [217] R. Gupta, I. Elamvazuthi, S. C. Dass, I. Faye, P. Vasant, J. George, and F. Izza, "Curvelet based automatic segmentation of supraspinatus tendon from ultrasound image: a focused assistive diagnostic method," *Biomed. Eng. online2*, vol. 13, no. 1, p. 157, 2014.
- [218] C. Bottomley and T. Bourne, "Dating and growth in the first trimester," *Best Pract. Res. Clin. Obstet. Gynaecol.*, vol. 23, no. 4, pp. 439–452, 2009.
- [219] J. Sonek, "First trimester ultrasonography in screening and detection of fetal anomalies," in *American Journal of Medical Genetics Part C: Seminars in Medical Genetics*, 2007, vol. 145, no. 1, pp. 45–61.
- [220] S. Rueda, S. Fathima, C. L. Knight, M. Yaqub, A. T. Papageorgiou, B. Rahmatullah, A. Foi, M. Maggioni, A. Pepe, J. Tohka, R. V Stebbing, J. E. McManigle, A. Ciurte, X. Bresson, M. B. Cuadra, S. Changming, G. V Ponomarev, M. S. Gelfand, M. D. Kazanov, W. Ching-Wei, C. Hsiang-Chou, P. Chun-Wei, H. Chu-Mei, and J. A. Noble, "Evaluation and comparison of current fetal ultrasound image segmentation methods for biometric measurements: a grand challenge," *Med. Imaging, IEEE Trans.*, vol. 33, no. 4, pp. 797–813, 2014.
- [221] L. Zhang, X. Ye, T. Lambrou, W. Duan, N. Allinson, N. J. Dudley, M. M. F. C. and M. J. Arbelaez P, B. J. M. and A. D. G, G. B. and G. S. Carneiro G, G. B. G. S. and C. D. Carneiro G, C. S. K. N. N. M. and G. M. Chaudhuri S, B. X. and C. M. B. Ciurte A, R. S. B. X. N. S. P. A. T. N. J. A. and B. C. M. Ciurte A, D. N. J. and C. E, G. S. R. E. and L. W. Espinoza J, P. M. and F. R. B. Fitzgibbon A W, M. M. P. A. R. S. N. J. A. P. A. T. and T. J. Foi A, S. K. and D. I. Haralick R M, H. T. et al, J. S. M. and F. M. A, J. B, L. T. and M. J, C. L. E. T. and C. T. Loughna P, T. J. L. and F. R. Lu W, B. S. S. J. and L. T. Malik J, F. C. C. and M. J. Martin D R, N. A. I. L. and N. J. A, B. I. and W. E. Pemberton L K, P. P. and M. J, P. N, P. N. and K. P, R. S. et al, A. R. S. and K. V Shrimali V, S. R. V. and M. J. E, L. V. R. Y. Z. G. I. C. S. H. C. L. M. H. B. E. and W. J. Udupa J K, V. M. and Z. A, W. J, W. J, W. Y. Y. and C. P. Yu J H, Y. Y. M. K. L. M. and K. Y. Zhang F, and G. C. E. W. Y. Z. and X. Z. J. Zhu S C, "A supervised texton based approach for automatic segmentation and measurement of the fetal head and femur in 2D ultrasound images," *Phys. Med. Biol.*, vol. 61, no. 3, pp. 1095–1115, Feb. 2016.
- [222] A. Foi, M. Maggioni, A. Pepe, and J. Tohka, "Head contour extraction from fetal ultrasound images by difference of Gaussians revolved along elliptical paths," in *Proceedings of Challenge US: Biometric Measurements from Fetal Ultrasound Images, ISBI 2012*, 2012, pp. 1–3.
- [223] A. Ciurte, X. Bresson, and M. Cuadra, "A semi-supervised patchbased approach for segmentation of fetal ultrasound imaging," in *proceedings of Challenge US: Biometric Measurements from Fetal Ultrasound Images, ISBI 2012*, 2012, pp. 5–7.

- [224] C. Sun, "Automatic fetal head measurements from ultrasound images using circular shortest paths," *Proc. Chall. US Biometric Meas. from Fetal Ultrasound Images, ISBI 2012*, pp. 13–15, 2012.
- [225] R. Stebbing and J. McManigle, "A boundary fragment model for head segmentation in fetal ultrasound," in *Proceedings of Challenge US: Biometric Measurements from Fetal Ultrasound Images, ISBI 2012*, 2012, pp. 9–11.
- [226] C. Wang, H. Chen, C. Peng, and C. Hung, "Automatic femur segmentation and length measurement from fetal ultrasound images," *Proc. Chall. US Biometric Meas. from Fetal Ultrasound Images, ISBI 2012*, pp. 21–23, 2012.
- [227] Y. Deng, Y. Wang, P. Chen, and J. Yu, "A hierarchical model for automatic nuchal translucency detection from ultrasound images," *Comput. Biol. Med.*, vol. 42, no. 6, pp. 706–713, 2012.
- [228] P. Chen, M. Chen, and T. Leung, "Effect of image settings on nuchal translucency thickness measurement by a semi-automated system," *Ultrasound Obstet. Gynecol.*, vol. 39, no. 2, pp. 169–174, 2012.
- [229] Y. Lee, M. Kim, and M. Kim, "Robust border enhancement and detection for measurement of fetal nuchal translucency in ultrasound images," *Med. Biol. Eng. Comput.*, vol. 45, no. 11, pp. 1143–1152, 2007.
- [230] J. Moratalla, K. Pintoffl, and R. Minekawa, "Semi-automated system for measurement of nuchal translucency thickness," *Ultrasound Obstet. Gynecol.*, vol. 36, no. 4, pp. 412–416, 2010.
- [231] L. Wee, T. Min, and A. Arooj, "Nuchal translucency marker detection based on artificial neural network and measurement via bidirectional iteration forward propagation," *WSEAS Trans. Inf. Sci. Appl.*, vol. 7, no. 8, pp. 1025–1036, 2010.
- [232] B. Gutiérrez-Becker, F. A. Cosío, M. E. G. Huerta, L. Benavides-Serralde, J.A., Camargo-Marín, and V. M. Bañuelos, "Automatic segmentation of the fetal cerebellum on ultrasound volumes, using a 3D statistical shape model," *Med. Biol. Eng. Comput.*, vol. 51, no. 9, pp. 1021–1030, 2013.
- [233] G. Velásquez-Rodríguez, F. Arámbula Cosío, and B. Escalate Ramírez, "Automatic segmentation of the fetal cerebellum using spherical harmonics and gray level profiles," in *11th International Symposium on Medical Information Processing and Analysis (SIPAIM 2015)*, 2015, p. 968114.
- [234] D. Ni, T. Li, X. Yang, J. Qin, S. Li, C.-T. Chin, S. Ouyang, T. Wang, and S. Chen, "Selective search and sequential detection for standard plane localization in ultrasound," *Abdom. Imaging Comput. Clin. Appl.*, vol. 8198, pp. 203–211, 2013.
- [235] H. Chen, D. Ni, J. Qin, S. Li, X. Yang, T. Wang, and P. A. Heng, "Standard plane localization in fetal ultrasound via domain transferred deep neural networks," *IEEE J. Biomed. Heal. Informatics*, vol. 19, no. 5, pp. 1627–1636, 2015.
- [236] G. Tarroni, S. Visentin, E. Cosmi, and E. Grisan, "Fully-automated identification and segmentation of aortic lumen from fetal ultrasound images," in *2015 37th Annual International Conference of the IEEE Engineering in Medicine and Biology Society (EMBC)*, 2015, pp. 153–156.
- [237] G. Tarroni, S. Visentin, E. Cosmi, and E. Grisan, "A novel approach to aortic intima-media thickness quantification from fetal ultrasound images," in *2015 IEEE 12th International Symposium on Biomedical Imaging (ISBI)*, 2015, pp. 858–861.
- [238] D. Bibicu, L. Moraru, and M. Stratulat (Visan), "Diagnostic accuracy of ovarian cyst segmentation in B-mode ultrasound images," in *AIP Conference Proceedings*, 2013, vol. 1564, pp. 164–170.

- [239] Q. Zheng, Y. Liu, and W. Zhu, "Uterine calcifications segmentation and extraction from ultrasound images based on level set," in *Information Management, Innovation Management and Industrial Engineering (ICIII)*, 2013, pp. 6–9.
- [240] B. Ni, F. He, and Z. Yuan, "Segmentation of uterine fibroid ultrasound images using a dynamic statistical shape model in {HIFU} therapy," *Comput. Med. Imaging Graph.*, vol. 46, Part 3, pp. 302–314, 2015.
- [241] T. R. Jeyalakshmi and K. Ramar, "Segmentation of uterine fibroid using morphology: An automatic approach," *2009 Int. Conf. Intell. Agent Multi-Agent Syst. IAMA 2009*, pp. 1–6, 2009.
- [242] R. Saranya and S. U. Maheswari, "Follicle detection in ovary image using adaptive particle swarm optimization," *J. Med. Imaging Heal. Informatics*, vol. 6, no. 1, pp. 125–132, 2016.
- [243] B. Padmapriya and T. Kesavamurthy, "Detection of follicles in poly cystic ovarian syndrome in ultrasound images using morphological operations," *J. Med. Imaging Heal. Informatics*, vol. 6, no. 1, pp. 240–243, 2016.
- [244] B. Potočník and D. Zazula, "Automated ovarian follicle segmentation using region growing," in *International Symposium on Image and Signal Processing and Analysis, ISPA*, 2000, pp. 157–162.
- [245] D. Zhang, Y. Liu, Y. Yang, M. Xu, Y. Yan, and Q. Qin, "A region-based segmentation method for ultrasound images in HIFU therapy," *Med. Phys.*, vol. 43, no. 6, pp. 2975–2989, 2016.
- [246] S. Nouranian, M. Ramezani, I. Spadinger, W. J. Morris, S. E. Salcudean, and P. Abolmaesumi, "Learning-Based Multi-Label Segmentation of Transrectal Ultrasound Images for Prostate Brachytherapy," *IEEE Trans. Med. Imaging*, vol. 35, no. 3, pp. 921–932, 2016.
- [247] Dinggang Shen, Yiqiang Zhan, and C. Davatzikos, "Segmentation of prostate boundaries from ultrasound images using statistical shape model," *IEEE Trans. Med. Imaging*, vol. 22, no. 4, pp. 539–551, Apr. 2003.
- [248] C. Knoll, M. Alcañiz, V. Grau, C. Monserrat, and M. Carmen Juan, "Outlining of the prostate using snakes with shape restrictions based on the wavelet transform (Doctoral Thesis: Dissertation)," *Pattern Recognit.*, vol. 32, no. 10, pp. 1767–1781, Oct. 1999.
- [249] L. Gong, S. D. Pathak, D. R. Haynor, P. S. Cho, and Y. Kim, "Parametric shape modeling using deformable superellipses for prostate segmentation," *IEEE Trans. Med. Imaging*, vol. 23, no. 3, pp. 340–349, Mar. 2004.
- [250] R. P. Singh, S. Gupta, and U. R. Acharya, "Segmentation of prostate contours for automated diagnosis using ultrasound images: A survey," *J. Comput. Sci.*, 2017.
- [251] Y. J. Liu, W. S. Ng, M. Y. Teo, and H. C. Lim, "Computerised prostate boundary estimation of ultrasound images using radial bas-relief method," *Med. Biol. Eng. Comput.*, vol. 35, no. 5, pp. 445–454, Sep. 1997.
- [252] S. Ghose, A. Oliver, R. Martí, X. Lladó, J. Freixenet, J. Mitra, J. C. Vilanova, J. Comet, and F. Meriaudeau, "Multiple mean models of statistical shape and probability priors for automatic prostate segmentation," Springer, Berlin, Heidelberg, 2011, pp. 35–46.
- [253] H. M. Ladak, F. Mao, Y. Wang, D. B. Downey, D. A. Steinman, and A. Fenster, "Prostate boundary segmentation from 2D ultrasound images," *Med. Phys.*, vol. 27, no. 8, pp. 1777–1788, Aug. 2000.
- [254] D. Shen, Y. Zhan, and C. Davatzikos, "Segmentation of prostate boundaries from ultrasound images using statistical shape model," *IEEE Trans. Med. Imaging*, vol. 22, no. 4, pp. 539–551, Apr. 2003.

- [255] B. Chiu, G. H. Freeman, M. M. A. Salama, and A. Fenster, "Prostate segmentation algorithm using dyadic wavelet transform and discrete dynamic contour," *Phys. Med. Biol.*, vol. 49, no. 21, pp. 4943–4960, Nov. 2004.
- [256] F. A. Cosìo, "Automatic initialization of an active shape model of the prostate," *Med. Image Anal.*, vol. 12, no. 4, pp. 469–483, Aug. 2008.
- [257] P. Yan, S. Xu, B. Turkbey, and J. Kruecker, "Adaptively learning local shape statistics for prostate segmentation in ultrasound," *IEEE Trans. Biomed. Eng.*, vol. 58, no. 3 PART 1, pp. 633–641, Mar. 2011.
- [258] P. Wu, Y. Liu, Y. Li, and Y. Shi, "TRUS image segmentation with non-parametric kernel density estimation shape prior," *Biomed. Signal Process. Control*, vol. 8, no. 6, pp. 764–771, Nov. 2013.
- [259] P. Wu, Y. Liu, Y. Li, and B. Liu, "Robust prostate segmentation using intrinsic properties of TRUS images," *IEEE Trans. Med. Imaging*, vol. 34, no. 6, pp. 1321–1335, Jun. 2015.
- [260] I. Dydenko, D. Friboulet, J. M. Gorce, J. D'hooge, B. Bijmens, and I. E. Magnin, "Towards ultrasound cardiac image segmentation based on the radiofrequency signal," *Med. Image Anal.*, vol. 7, no. 3, pp. 353–367, 2003.
- [261] D. Boukerroui, A. Baskurt, J. Noble, and O. Basset, "Segmentation of ultrasound images—multiresolution 2D and 3D algorithm based on global and local statistics," *Pattern Recognit. Lett.*, vol. 24, no. 4, pp. 779–790, 2003.
- [262] E. Von Lavante and J. A. Noble, "Segmentation of breast cancer masses in ultrasound using radio-frequency signal derived parameters and strain estimates," in *2008 5th IEEE International Symposium on Biomedical Imaging: From Nano to Macro, Proceedings, ISBI, 2008*, no. May 2014, pp. 536–539.
- [263] I. Despotovic and B. Goossens, "Using phase information in ultrasound RF-signals for tissue characterization," in *Annual work-shop on Circuits, Systems and Signal Processing (ProRISC 2008)*, 2008, pp. 314–317.
- [264] C. Azzopardi, K. P. Camilleri, and Y. A. Hicks, "Carotid ultrasound segmentation using radio-frequency derived phase information and gabor filters," in *Proceedings of the Annual International Conference of the IEEE Engineering in Medicine and Biology Society, EMBS, 2015*, vol. 2015–Novem, pp. 6338–6341.
- [265] J. Stoitsis, S. Golemati, S. Kendros, and K. S. Nikita, "Automated detection of the carotid artery wall in B-mode ultrasound images using active contours initialized by the Hough transform," in *2008 30th Annual International Conference of the IEEE Engineering in Medicine and Biology Society, 2008*, pp. 3146–3149.
- [266] D. Boukerroui, O. Basset, and A. Baskurt, "A multiparametric and multiresolution segmentation algorithm of 3D ultrasonic data," *IEEE Trans. Ultrason. Ferroelectr. Freq. Control*, vol. 48, no. 1, pp. 64–77, 2001.
- [267] M. Nillesen, R. Lopata, and H. Huisman, "Correlation based 3-D segmentation of the left ventricle in pediatric echocardiographic images using radio-frequency data," *Ultrasound Med. Biol.*, vol. 37, no. 9, pp. 1409–1420, 2011.